Marine Geology
September 2022, Volume 451 Pages 106883 (17p.)
https://doi.org/10.1016/j.margeo.2022.106883
https://archimer.ifremer.fr/doc/00788/89986/

Archimer
https://archimer.ifremer.fr

Late Pleistocene- Holocene architecture and sedimentary processes on the glacially influenced SW Grand Banks Slope off Newfoundland

Gao Ya [1, 2, 3, *], Piper David J.W. [2, 4], Normandeau Alexandre [2], Xie Xinong [1, 5]

[1] Hubei Key Laboratory of Marine Geological Resources, China University of Geosciences (CUG), Wuhan 430074, PR China
[2] Natural Resources Canada, Geological Survey of Canada (Atlantic), Bedford Institute of Oceanography, P.O. Box 1006, Dartmouth, Nova Scotia B2Y 4A2, Canada
[3] Guangdong Provincial Key Laboratory of Marine Resources and Coastal Engineering, Guangzhou, Guangdong 510006, PR China
[4] Department of Oceanography, Dalhousie University, Halifax, Nova Scotia B3H 4R2, Canada
[5] Southern Marine Science and Engineering Guangdong Laboratory (Zhuhai), Zhuhai, 519082, China

* Corresponding author : Ya Gao, email address : yagao@cug.edu.cn

Abstract :

Complex inter-relationships between alongslope and downslope sediment dispersion exist on glaciated continental margins and vary widely along continental margins depending on sediment supply and bottom current strength. In eastern Canada, proglacial sedimentation rates are relatively high on the SW Grand Banks Slope compared to the sediment starved SE Grand Banks margin, but relatively low compared to the glacially dominated Scotian margin off eastern Canada. As on other parts of the Canadian margin, its late Quaternary sediment architecture has been constructed by interacting alongslope and downslope processes. These include sediment transported by downslope glacial meltwater discharge, alongslope bottom currents and ice-rafting. Based on the analysis of sediment cores going back to 24 ka (Heinrich event 2), this study investigates fine-grained sedimentary facies and the development of variable depositional patterns on the glacially influenced SW Grand Banks Slope off Newfoundland (eastern Canada). Both turbidites and contourites show stratification, but differ in internal structure, the presence of IRD, and the nature of their upper and lower boundaries. Sandy contourites are mostly massive, occurring either as lenses or as part of the ideal bi-gradational vertical sequence with mottled silt-mud. Glacial silty contourites have distinct rhythmic laminae with the long axis of IRD parallel to bedding. Regional scale thickness variations allow discrimination between hemipelagites and muddy contourites. Depositional architecture is built through temporal and spatial coupling of the diverse sedimentary processes. During the last glacial maximum and early deglaciation, turbidity currents fed either by meltwater or oceanographic processes flowed in canyons, and a contourite depositional system developed between the canyons. The two systems interacted on inter-canyon ridges, where contourite sedimentation was not completely overwhelmed by energetic turbidity currents. In the Holocene, alongslope processes became dominant, building a drift with clearly variable thickness, in part related to seabed morphology. A conceptual model is proposed to present the key elements of depositional

Please note that this is an author-produced PDF of an article accepted for publication following peer review. The definitive publisher-authenticated version is available on the publisher Web site.

processes in this depositional system, and a similar evolutionary history can be expected on other distal glacial margins.

Highlights

► Sediment processes and architecture from local sediment input and bottom currents. ► Changing meltwater availability from the southeastern Laurentide Ice Sheet. ► Intercanyon ridges record turbidite-contourite interaction. ► Holocene drift-building responded to bottom current interaction with topography.

Keywords : Fine-grained facies, Contourite, Turbidite, Mixed and hybrid systems, Ice -rafted detritus, Labrador current

Please note that this is an author-produced PDF of an article accepted for publication following peer review. The definitive publisher-authenticated version is available on the publisher Web site.

1. Introduction

Glaciation and its related processes modulate climate change, sculpt continental margins and transport vast quantities of sediment, therefore having a profound effect on margin sedimentation. Much of the eastern Canadian margin has experienced repeated glaciation in the Quaternary, giving rise to numerous u-shaped troughs and tunnel valleys across the continental shelf (Piper, 1988; Boyd et al., 1988; MacRae and Christians, 2013). Those transverse troughs were occupied by fast-flowing ice streams from the continent, and topographically acted as the major paths of meltwater discharge, whereas tunnel-valleys transferred large quantities of subglacial meltwater to the continental margin (Skene and Piper, 2003; Shaw et al., 2006; Tripsanas and Piper, 2008; Piper et al., 2012; Roger et al., 2013) The direct effects of glaciation on the continental slopes therefore are the increased downslope sediment supply, likely further expressed by the occurrence of sediment gravity flows. At the same time, material transported to deep-water environments is also dispersed by alongslope currents, developing contourite depositional systems.

During the last glacial cycle, the Laurentide ice-sheet (LIS) extended some 200 km from the shoreline onto the inner part of the Grand Banks of Newfoundland (Fig. 1). Indeed, downslope processes enhanced by significant proglacial sediment supply dominated sedimentation on the Scotian margin and at Halibut canyon (Normandeau and Campbell, 2020; Tang and Piper, 2020), where ice crossed the shelf break at around the global last glacial maximum (LGM). However, around the Grand Banks slope, previous studies show that the southeast sector of LIS was remote from the SE Grand Banks shelf and slope (Shaw et al., 2006; Dalton et al., 2020), leaving the SE Grand Banks Slope sediment starved and current-swept (Rashid et al., 2019). An intermediate situation prevailed on the SW Grand Banks, where the southeastern part of LIS crossed the inner part of the Grand Banks. Although the icesheet failed to extend to the shelf break, meltwater discharge reaching the shelf break affected slope sedimentation (e.g., Lucchi and Rebesco, 2007; Tripsanas and Piper, 2008; Normandeau and Campbell, 2020). Nevertheless, the extent to which meltwater availability influences the architecture of slope deposits on the SW Grand Banks is still poorly evaluated. The relatively balanced forces of sweeping along-slope currents and gravity-driven down-slope flows provide a sedimentary archive of their interaction.

In this study, we analyzed six sediment cores, with the aims of (1) identifying Late Pleistocene-Holocene lithofacies and distinguishing the various origins of fine-grained sedimentary facies; (2) investigating the temporal and spatial distribution of downslope and along-slope sedimentation on the SW Grand Banks slope; (3) establishing the character of sediment facies where there is a record of the interaction of downslope and along-slope processes on intercanyon ridges; and (4) assessing how meltwater availability and bottom currents characterize depositional phases since the late Pleistocene. These results allow us to establish conceptual models for sediment dynamics in a changing depositional environment, and to understand how a variety of processes have influenced the SW Grand Banks slope architecture.

2. Geological setting

2.1 Tectonic and geological background

The Grand Banks of Newfoundland, as a broad zone of extension in southeastern Canada (Fig. 1A), was produced from renewed asymmetric rifting of the Grand Banks from Iberia in the late Jurassic. The old SW Grand Banks transform continued into the Newfoundland-Azores-Gibraltar Fracture Zone (Pe-Piper et al., 2007). The Grand Banks are underlain by thick Jurassic, Cretaceous and Cenozoic strata overlying Triassic salt (Wade & MacLean, 1990). The slope extends from the shelf break at a water depth of 100-150 m to ~2500 m (Piper, 2005). The Grand Banks have experienced westward tectonic tilting, so that the Quaternary sequence (upper 100 m) on the SW side is much thicker than on the SE side, and unconformably overlies a progradational Cenozoic succession several hundred metres thick (Grant and McAlpine, 1990). Episodic ice sheet advances deposited glacial till on the shelf and upper slope, down to a water depth of about 600 m (Piper et al., 2012).

The study area, between 54°W to 53°E, 44°N to 44.5°N, is located in water depths between ~700 m and ~1600 m (Fig. 1B). It is dissected by two submarine canyons: 1) the large DesBarres Canyon (Fig 1B), which has several heads that incise the shelf, and 2) a slope-confined canyon to the northwest, informally known as "Narwhal Canyon", which is of a smaller scale with its heads in 400-600 metres below sea level. The regional morphology was considerably influenced by glacial processes, as Piper and Gould (2004) demonstrated that canyon-widening events south of Whale Bank were synchronous in multiple canyons and correlated approximately with the LGM ice advance.

2.2 Regional stratigraphy

Throughout the last glacial period, the major Hudson Strait ice stream discharged massive volumes of icebergs and meltwater during H-events (Broecker et al., 1992; Andrews and Voelker, 2018), derived from erosion of Paleozoic carbonates in Hudson Bay. Suspended sediment and icebergs were further advected great distances by along-slope currents along the margin (Andrews and Tedesco, 1992; DeGelleke et al., 2013), depositing so-called H-layers rich in ice-rafted detritus (IRD) and detrital carbonate. The recognition of H-layers thus has been applied to establish the stratigraphic framework for many core studies on the eastern Canadian margin (e.g., Hundert and Piper, 2008; Tripsanas et al., 2008; Mao et al., 2018; Rashid et al., 2019).

2.3 Local ice maximum advance at LGM

At LGM, there are limited data that clearly define the timing of maximum ice advance from the Scotian margin to the study area (Fig. S1). Seaward of the central Scotian Slope, till tongues representing maximum ice advance are overlain by regional seismic reflections (Fig. S2) that are dated from nearby cores at 24.5 ka and 27.5 ka (Supplementary Table T1; all reported ages are calibrated). Seaward of Laurentian Channel, the shallowest till tongue has an age of 19 ka (Piper and Macdonald, 2001). Seaward of St. Pierre Bank, the base of the youngest till can be traced downslope to its pinchout in seismic profiles (Fig. S3), where it is dated from nearby cores at 17.8–18.2 ka. Locally, ice extended as far as > 500 m water depth at this time and remained in place during early deglaciation (Bonifay and Piper, 1988). In Halibut Channel, a wedge-shaped till tongue is dated at ~11.9 ka (Fig. S4), indicating that ice occupied part of the channel to as late as the Younger Dryas episode (Miller et al., 1991; Cameron and King, 2011). On the upper slope south of DesBarres canyon, the base of youngest till is correlated to a regional reflector with an age of ~ 60 ka (Piper and Gould, 2004). A reflector corresponding to just below H2 (~25 ka) cannot be traced further upslope (Fig. S5). So while there is widespread evidence for shelf crossing ice between 25 and 19 ka on the Scotian margin, Laurentian Channel and St Pierre Bank, ice did not cross shelf break at LGM in the study area. A recent glacial reconstruction proposed by Dalton et al. (2020, 2022) (Fig. 1A) shows ice extending onto Whale Bank at LGM, but retreating to near the present coastline by 18.7 ka. Thus the southern portion of Grand Banks is not believed to have been ice covered in marine isotope stage (MIS) 2, but was emergent during lowered sea level (Shaw et al. 2006) and thus crossed by glacial meltwater.

2.4 Oceanographic setting

The northwest Atlantic continental margin is swept by the Labrador Current (LC) and the Western Boundary Undercurrent that flows in water depths greater than about 4000 m (Cochonat et al., 1989). The LC is a continuation of the Western Greenland and Baffin Island currents and is divided into two branches: the colder and less saline inner Labrador Current flows along the Labrador and NE Newfoundland shelves and through Avalon Channel, and the warmer, more saline outer LC flows at a water depth down to the continental slope (Fig. 1A). The outer LC splits north of Flemish Cap, with the main component flowing along the outer margin east of Flemish Cap and a slightly lesser amount of water flowing southwards through Flemish Pass (Fig. 1A). Further south, it flows around the Grand Banks where it meets warm Gulf Stream, with its main thread at least down to 1350 m on the SE Grand Banks (Rashid et al., 2019). At the Tail of the Bank, Fratantoni and Mccartney (2010) estimated that most of the equatorward baroclinic transport retroflects back toward the northeast, based on the annual mean distribution of salinity, leaving a lesser amount continuing along the SW Grand Banks margin including the study area.

3. Materials and methods

Six piston cores from the SW Grand Banks slope were used in this study (Table 1). Core 2031 was collected using a Calypso giant piston corer from *RV Marion Dufresne* in 1995, and other cores were collected by a AGC piston corer during CCGS *Hudson* cruises. Accompanying trigger weight cores are only available from the CCGS *Hudson* cruises. Each core was analyzed by a Geotek multi-sensor core logger to measure bulk density at an interval of 1 cm. Cores were then split, described, digitally photographed, X-rayed to better investigate the sedimentary structure and then kept refrigerated.

High-resolution digital colour data (CIELAB protocol of L*, a* and b*, L: luminance, a: green to red, b: blue to yellow) were measured at 1 cm intervals using a Minolta Spectrophotometer CM 2002 on cores 35, 34 and 2031, and a Minolta Spectrophotometer CM 2600d on all other cores. The calibration and principle are the same and apply to the whole colour space, but the CM 2002 gave higher a* values. An empirical equation relating the two instruments was developed:

$$a^*{}_{spectro\ CM\ 2600d} = \frac{a^*{}_{spectro\ CM\ 2002}}{1.2} - 1$$

Thus a* values collected by the Minolta Spectrophotometer CM 2002 were corrected to make them comparable.

The bulk geochemical composition was determined at 1 cm depth intervals, using an Innov-X Delta Premium 6000 portable X-ray fluorescence (pXRF) core scanner with a 30 s dwell time for each of beams 2 and 3. Light elements such as Al are not reliably determined by this technique. Four elements appear to be useful based on previous investigations: Ti is a common detrital mineral from some igneous, metamorphic and sedimentary rocks and may be common in both fine sand and mud fractions (Mao et al., 2014). K tends to be higher in fine fractions, but is also common in ice-rafted sediment derived from the Canadian and Greenland shields (Mao et al., 2014; Meng and Piper, 2020). Zr is concentrated in fine sands and coarse silts (Li and Piper, 2015). All three are sufficiently abundant that measurements are reasonably precise and not subject to the nugget effect. Ca may be biogenic in the later Holocene but is largely detrital from ice rafting (Li and Piper, 2015; Rashid et al., 2017). Element ratios are adopted to reduce the effects of water content in the sediment (Hennekam and De Lange, 2012).

Subsamples were taken for grain size at a variable spacing, ranging from 10 cm in the Holocene to 20 cm in the late Pleistocene. Grain size analyses were performed on bulk sediment with no chemical pre-treatment. A small amount of each sample was dispersed by ultrasonic treatment for about 10 s before measuring using a Beckman Coulter 231 LS 230 laser diffraction analyzer. Grain size data were processed using in-house software Particle Sizing System, whose principle is based on the method of Folk and Ward (1957). Sediment particles larger than 150 μm are considered to have been transported by ice-rafting (Andrews, 2000), so >150 μm% is adopted to give an estimate of the proportion of IRD.

Eleven new ^{14}C-accelerator mass spectrometer (AMS) dates were obtained on bivalve fragments or planktonic foraminifers with weights > 5 mg picked from >212 μm fraction to constrain the chronostratigraphy (Table 2). The radiocarbon dates were calibrated to calendar ages using CALIB 8.1 (Stuiver and Reimer, 1993) and the MARINE20 calibration dataset (Heaton et al., 2020) with ΔR = 144±35 years (McNeely et al. 2006). All dates refer to cal ka.

4. Results

4.1 Piston cores

Piston core 34, collected at a water depth (wd) of 716 m, is the shallowest core available from the upper part of the slope. Downslope, core 35 at 1326 m wd has a similar stratigraphy to core 34 (Fig. S6). They are both located upstream of DesBarres Canyon with respect to the northwestward flowing bottom current. A comparison of physical properties and pXRF of trigger-weight cores with the piston cores suggests that the upper 23 cm and 7 cm of piston cores 34 and 35 were missing, respectively (Fig. S7).

Core 16 was collected at 1349 m wd, close to a gully on an inter-canyon ridge in the head of DesBarres Canyon. It is located ~ 50 m higher than the gully floor and is 500-800 m higher than DesBarres Canyon thalweg. No trigger-weight core is available. Core 15 at 1045 m wd was collected from the continental slope northwest of DesBarres Canyon, with a <50 m deep gully on its NE side (Fig. S6). The section in the core is condensed and based on the trigger weight core the upper 53 cm of the piston core is missing (Fig. S7).

Cores 37 and 2031 were both taken near Narwhal Canyon, at a water depth between 1500 and 1600 m (Fig. S6). Core 37 is located on a terrace 86 m above the Narwhal Canyon floor, and its uppermost 25 cm was lost (Fig. S5). Core 2031 was collected from a ridge near Narwhal Canyon without a trigger-weight core. The softer sediments at its top appear to have suffered stretching during the coring process (Piper et al., 1999), typically showing 200% extension in the upper 4 m of sediments (Skene and Piper, 2003).

4.2 Lithofacies

Eight main lithofacies are recognized in the studied cores, on the basis of colour, grain size, the presence and distribution of IRD, and lithological structures (Figs. 2 and 3). Downcore photographs with X-radiographs, grain size distribution, physical properties and geochemical plots for core 34 and 37 are presented in Figures 4 and 5.

Lithofacies 1: Homogeneous mud

Lithofacies 1 (L1) has a bimodal grain size distribution, with a dominant peak at ~ 7-9 μm as fine silt and a relatively slight peak at ~30 μm as coarse silt (Fig. 2). Sand content is less than 10%. Mean grain size ranges from 5.4 to 9.4 μm. It mostly appears as m-thick structureless intervals, in places punctuated by cm-thick visible bioturbation (Fig. 2).

Homogeneous mud commonly occurs at the upper part of cores, characterized by a rising Ca/Ti ratio towards the core top (Fig. 6). K/Ti and Zr/Ti are relatively stable (Figs. 4 and 5).

Lithofacies 2: Mottled olive-grey silty mud with IRD

The sand content of L2 varies from 10% to ~28%. Grain-size distribution is mostly trimodal, with a major peak at 40-60 μm as very coarse silt (Fig. 2a). Mean grain size ranges from 8.2 to 22.1 μm. Variants of this lithofacies consist of 1) faint wavy-laminated silty layers or silt lenses with common IRD and indistinct boundaries; 2) rhythmic lamination comprising IRD-rich millimetre-scale wavy-parallel laminae, in which IRD is better sorted and preferentially layered within laminae, with long axes of clasts roughly parallel to bedding rather than with a random distribution; 3) centimetre-thick intervals with common finer and coarser grained IRD forming weakly to moderately stratified layers; 4) massive, with randomly scattered IRD.

This lithofacies is found mostly in the middle interval of cores, except cores 2031 and 37. Changing in bulk density, Ca/Ti, K/Ti and Zr/Ti are mostly gradually increased or decreased (e.g., 100-240 cm in core 34 (Fig. 4).

Lithofacies 3: Fine-grained dark grey sandy mud with IRD

The average sand content of L3 is ~30–45% with a mean grain size of 17.4–42.5 μm. Variants are 1) structureless with a few scattered IRD (Fig. 2), and locally with coarser-grained lenses; 2) with sub-horizontal to irregular surfaces with either sharp or indistinct boundaries, showing indistinct laminae containing shell fragments, where bed thickness is less than 10 cm.

L3 usually occurs as 10-40 cm thick beds, corresponding to increased Zr/Ti and decreased K/Ti. Ca/Ti is smooth but has higher values compared to L2. The shallowest development of L3 appears to correlate in all cores except in core 37 (Fig. 6).

Lithofacies 4: Alternating grey silty to sandy mud devoid of IRD

L4 contains a higher percentage of very fine sand compared to IRD-rich laminated layers and the major peak at ~100 μm in the grain size distribution is both coarser and more leptokurtic (Fig. 2). Variants comprise 1) finely laminated mud interbedded with finer-grained mud devoid of visible bioturbation; 2) well stratified sandy layers with sand content up to > 50%, which are interbedded with some silty to very fine sandy deposits containing sparse IRD; 3) normal-graded sequences (< 10 cm thick) with a sharp erosional base.

This lithofacies is not identified in cores 34 and 35, but is dominant in the middle of cores 37 and 2031 (Fig. 6). Density values remain relatively high and show abrupt changes. A similar pattern of rapid fluctuation is also observed in K/Ti and Zr/Ti (Fig. 5).

Lithofacies 5: Bioturbated olive green silty mud

L5 shows sediment homogenization from extensive bioturbation. Sand content is mostly

15–20%, giving a mean grain size in a narrow range from 13 to 16.5 µm. X-radiography failed to reveal any structure, because sediments were much disturbed by cracks from gas expansion. Scattered IRD is less abundant than in other grey silty mud (Fig. 3). The tiering structure of bioturbation was not confidently established, due to the narrow-exposed surface and low colour contrast in soft sediments, but overall the pattern of biogenic reworking shows an alternation of various ichnogenera, including *Planolites*, *Phycosiphon*, *Thalassinoides* and *Scolicia*, without any trace of deeper tier *Zoophycos*.

L5 is only found in core 16 below ~ 520 cm. Geochemical signatures such as Ca/Ti remain very stable without any prominent variation (Fig. 6).

Lithofacies 6: grayish-red mud with layered IRD

L6 is differentiated from other lithofacies by its distinctive redness in colour revealed by a*. Sand content ranges from ~ 3% to ~31%. It has gradational contacts and scattered IRD in the form of stones and mud clasts, as well as layers of concentrated IRD also occur (Fig. 3).

Unit thickness of L6 is generally 20–30 cm in cores 34 and 35, but is unique in core 15 where a long interval up to 1.9 m thick is present (Fig. 6). Intervals are low in Ca/Ti and Zr/Ti, but high in K/Ti (Fig. 4).

Lithofacies 7: Detrital carbonate-rich mud with IRD

Peaks in Ca/Ti and abundant IRD (Figs. 3 and 6) are distinctive for this lithofacies, which corresponds to detrital carbonate Heinrich layers (H-layers; Heinrich, 1988; Andrews and Tedesco, 1992). Base and top contacts are gradational based on colour (Fig. 3).

Lithofacies 8: Conglomerate with dispersed mud clasts

L8 contains clasts typically 5 cm in size, in places supported in a muddy matrix but locally clast supported (Fig. 6). It is found at 720-770 cm in core 34, where it shows a major Ca/Ti peak comparable to L7, based on which Piper and Gould (2004) interpreted it as the slumped equivalent of the H2 layer. Thinner layers (10-15 cm thick) at ~900 cm in both cores 34 and 35 have lower Ca/Ti.

4.3 Radiocarbon dates

Eleven dates were previously published (Table 2) and eleven additional dates were obtained to further refine the stratigraphy. Three of them were dated on paired bivalves, while all the others were on planktonic foraminifera. In some cases, samples were taken over 2–3 cm to get enough foraminiferas. In core 2031, with new dates obtained at 2060–2065 cm and 2220–2225 cm, two old dates on mollusk shell fragments are rejected: the date at 1730 cm shows age inversion and the date at 2335 cm appears to be too old. All accepted calibrated ages are shown with regional core stratigraphy in Figure 6.

4.4 Chronostratigraphic framework

The cores spanning different ages are confidently correlated, based on the recognition of H-layers as tie points (Fig. 6). The H-layers represent periods of high supply of detrital carbonate to the LC from the Hudson Strait ice stream, as shown by high Ca/Ti. H1 is bracketed by dates in cores 2031, 16 and 35; H2 is confirmed by an overlying date in cores 15 and 35. The correlatable occurrence of lithofacies 3 near the top of most cores is bracketed by dates in core 2031 and directly overlies dates in cores 16, 35 and 37 that show it corresponds approximately to the Younger Dryas (YD) period. The correlations are also supported by variations in a*, representing supply of detrital hematite-rich sediment from ice streams off northeastern Newfoundland, as discussed in detail below. Three main sedimentary stages are recognized: LGM-early deglaciation (H2–H1), deglaciation (H1–YD) and the Holocene.

Cores 34 and 35 have clear H1 and H2 or H2-equivalent layers. The value of Ca/Ti reaches 70–80 in H-layers. Between H2 and H1, two grayish-red layers are recognized: one (318-342 cm in core 35 and 428-448 cm in core 34) has the most distinct a* peak, whereas the other one closer to H2 is distinguished by a higher a* value on average (e.g., in cores 34 and 15). Between two grayish-red layers, the Ca/Ti curve has a concave feature in both cores, further confirming the initial correlation.

In core 16, only one Ca/Ti peak was identified, corresponding to the H1 layer as located between two dated points of 14.60 ka and 18.90 ka. Core 16 failed to penetrate the H2 layer. In contrast, core 15 is highly condensed, most obvious at 580-740 cm where Ca/Ti fluctuates rapidly, with a series of spikes up to a value of 70. Above 580 cm, there is no major peak of

Ca/Ti similar to that of H-layers in core 34 or 35, but only a moderate peak at 65–78 cm. We consider it as H1 rather than H0 (a Younger Dryas detrital carbonate layer recognized locally beneath Labrador Current: Rashid et al. 2011), according to the major peak of a* at 108-132 cm and the concave feature of Ca/Ti from 130 to 370 cm, which match the patterns in cores 34 and 35 between H1 and H2. A date of 23.86 ka at 395 cm is consistent with the proposed stratigraphy.

The H1 layer in core 2031 is at 1015–1055 cm, and there is no Ca/Ti peak below it indicating H2. The radiocarbon date of 23.08 ka BP obtained from 2220-2225 cm demonstrates that H2 is near or just below the bottom of the core. In core 37, the Ca/Ti value remains low below 300 cm without any peak comparable to the H-layers. A date of 12.74 ka at 565 cm corresponds to the YD (Lowe et al., 2008), which suggests that the H1 layer may be located below the bottom of core 37.

Cores from Orphan Basin, upstream in the Labrador Current, show a correlatable series of red mud beds distinguished by high a* peaks between H3 and H1 (Tripsanas and Piper, 2008). Five of these peaks are distinguished in cores 34 and 35, including GR1 coincident with H1 and GR7 and 8 below H2 (Fig. 6). Some of these peaks are correlated to cores 15 and 16.

The YD interval was a period of rapid cooling in the Northern Hemisphere between ca. 12.8 and 11.6 ka BP (Andrews et al. 1995; Rasmussen et al., 2006), and its termination serves as a marker for the base of the Holocene. There is a sandy layer (or silty layer from cores at deeper water depth) in all cores corresponding to L3 (Fig. 6), distinguished from overlying mud-dominated sediment in the Holocene. Those sandy layers also correspond to the shallowest IRD maximum in each core, and serve as markers of the YD that can be well correlated across the region. The correlation is further confirmed by our dating of 11.78 ka at the top of a sandy layer from core 2031 and 12.81 ka below a sandy layer from core 35.

5. Interpretation and discussion

5.1 Distinguishing fine-grained sedimentary facies

5.1.1 Contourites

Contourites were originally defined as sediments deposited in the deep sea by along-slope bottom currents driven by thermohaline circulation. The term has been extended to accept a wider range of sediments deposited, significantly affected or substantially reworked by quasi-continuous bottom currents (Stow et al., 2002; Rebesco et al., 2014; Stow and Smillie, 2020). Here this widened definition was adopted.

Muddy contourites consist of light olive-grey muddy intervals, found in the upper parts of all cores (Fig. 3). They appear to be homogeneous except where bioturbation is visible. These features can equally be interpreted as hemipelagites or muddy contourites, making it difficult to distinguish at core scale (Nishida, 2016). Nevertheless, large regional variation in thickness favour a contourite origin: Holocene thickness is ~ 100 cm in cores 34 and 35, ~50-60 cm in core 15 and at deeper water depths, ~210 cm in core 2031 and > 300 cm in core 37 (Fig. 3). The different sedimentation rates are not likely to be caused by turbidites because they were not identified in all cores. A hemipelagite origin is also unlikely because the Holocene interval becomes thinner upslope. Numerous modelling studies have shown that alongslope mean flow is highly variable in location, direction and velocity around the Grand Banks of Newfoundland (Petrie and Isenor, 1985; Han et al., 2008; Li et al., 2015; Wang et al., 2015), which can yield variable sedimentation rates in contourite deposits (Stow et al., 2008; Rebesco et al., 2014). Lower sedimentation rate can be generated where flow speed is sufficient to keep most sediments in suspension and inhibit deposition, especially among muddy sediments. A similar trend was seen in cores mid to late Holocene in age around Flemish Cap (Piper et al., 2021). We thus infer that current vigor is the main cause for varied Holocene sedimentation rates, leading to muddy contourites as the interpretation for widespread Holocene mud. Observations from the middle slope of the continental margin off NE Argentina, with a regional thickness variation in muddy contourites (Bozzano et al., 2011) supports this interpretation.

Silty contourites have relatively distinct lamination resulting from the depositional sorting mechanism, in contrast to muddy contourites that have insufficient current velocity to generate depositional structures,. Laminae differs from those generated by turbidity currents by their general irregularity and discontinuity character and the presence of IRD. The observed rhythmic laminae (Fig. 2), may be similar to laminated mud deposited by meltwater plumes or nepheloid layers (e.g., Hesse et al., 1997; Lucchi and Rebesco, 2007), but more abundant IRD are found at the base and vary in size in the latter (e.g., Tripsanas and Piper, 2008; Jenner et al., 2018). Particularly well-aligned IRD observed in this study indicates a current depositional process as studied by Chough and Lee (1984), which is attributable to the effects of bottom currents (Ellwood and Ledbetter, 1977). The irregularly winnowed concentration of lenses at a centimetre scale and the widely spaced appearance of this facies is concordant with the interpretation.

Fine-grained sandy contourites are characterized by a notable absence of primary sedimentary structures. Where thickness is more than 30 cm, beds are mostly massive with gradual and indistinct boundaries, in places showing faintly rare lamination and bioturbation. Irregular lenses containing shell fragments as bioclasts are generally less than 5 cm thick, with boundaries clearer than those of structureless sand, along which dispersed IRD that show parallel orientation of clasts. None of these sandy beds are graded. All these distinctive sedimentary features indicate that these sands are contourites. Similar features of sandy contourites have been documented at the Gulf of Cadiz (Nelson et al., 1993; Stow et al., 2013) and the lower slope of the Faroe–Shetland Channel (Masson et al., 2010).

Following this interpretation, it is found that where the deposition was not overwhelmed by turbidites, the YD period is characterized by the appearance of regionally developed sandy contourites (Fig. 6). These sandy contourites, together with the overlying and underlying finer-grained deposits, constitute a sequence that is coarsening upward from muddy to bioturbated silty mud with indistinct laminae to structureless sandy mud, and then fining up through mottled silt with faint laminae back to muddy deposits, corresponding to gradual changing density, Ca/Ti, K/Ti and Zr/Ti (Fig. 7). The reverse-normal grading associated with faintly laminated silt and bioturbated mud is comparable to ideal bi-gradational facies model from divisions C1–C5 established for fine-grained mud-sand contourites (Faugères et al., 1984; Stow et al., 2002; 2008). The vertical arrangement of facies reflects changing current speed and/or sediment supply at a millennial time scale.

Possible processes that provide sediment to the margin include: 1) deglacial isostatic movements of the Newfoundland and Grand Banks, where in the latter area late glacial short time emergence presumably was subsequently followed by Holocene submergence (Liverman 1994), which may have favored the input of coarser material during YD; 2) storminess on the shelf could also have provided coarse sediments since storms were common in the YD (Toomey et al., 2017) and storm transport off the Grand Banks was predominantly to the SW (Li et al., 2017); 3) in a related manner, increased wave action on the shelf and upper slope caused by rapid sea ice decline during the late YD (Pearce et al., 2013) could have provided coarse sediment to the margin. On the other hand, during the early YD, large freshwater outbursts were triggered and poured into North Atlantic, disrupting the thermohaline circulation and allowing sea ice to form (Marchitto and Broecker, 2006; Murton et al., 2010). Enhancement of meltwater supply from ice sheets would intensify the Labrador Current (Pearce et al., 2014; Li and Piper, 2015), forming sandy contourites, corresponding to the maximum of current speed during the YD upstream in Flemish Pass (Li and Piper, 2015). At the base of the YD interval, laminated sandy contourite facies, which are most distinct in cores 34 and 35, show parallel and rhythmic lamination (Fig. 8c, d), and tend to form cycles of deposition, non-deposition and/or erosion during contourite accumulation in response to flow variability. Thus while input of sandy sediment from the shelf may have increased during the YD, the main observed sedimentary features result from increased current speed.

5.1.2 Turbidites

Turbidites were recognized by visual observations on X-radiographs and from physical properties data. Distinct beds of higher sand or silt concentration, with sharp or erosional basal contacts, drastically changing bulk density and normal grading, are the most common diagnostic criteria for turbidites in cores (e.g., Toucanne et al., 2008; Normandeau and Campbell, 2020; Stow and Smillie, 2020). On glacial margins, while semi-continuous contourite accumulation occurs contemporaneously with release of IRD, turbidity currents are episodic events with high sedimentation rate and commonly devoid of IRD. The observed interbedded mud lacking planktonic foraminifera and well-defined coarse silt or sand deposits without IRD are also distinctive characteristics of turbidites (e.g., Hesse and Khodabakhsh, 1998; Roger et al., 2013). Turbidites can also lead to age inversion, as observed at 1730 cm in core 2031, indicating the downslope transport of older material.

5.1.3 Hybrid deposits

Hybrid deposits are produced when multiple sedimentary processes interact, generally showing varied characteristics that cannot be related to the predominance of a typical single process. The olive green silty mud below ~ 520 cm in core 16 is interpreted to be a hybrid deposit, based on the following evidence: 1) core 16 has a thicker interval from H2 to H1, showing a much higher sedimentation rate than that in cores 34 and 35; 2) In comparison with cores 15, 34 and 35, in core 16 the a* peak values of identified grayish-red beds below H1 are less pronounced, indicating some dilution from local extra downslope sediment supply rather than reduced alongslope supply with distance (Fig. 6); 3) the core is located ~50 m higher than a gully floor, a height that allows overspill from some turbidity currents; 4) below 520 cm, where bioturbation is abundant throughout the silty mud, the trace fossil assemblage consists of tentatively identified *Planolites*, *Phycosiphon*, *Scolicia* and *Thalassinoides*. The deep tiering *Zoophycos* is lacking, meaning the upper tiers were not overprinted, which requires organic matter to be buried in time to prevent oxidation and allow the development of shallow or middle tier dwelling structures (Dorador et al., 2019). Taking all these points into consideration, it seems appropriate to interpret the bioturbated mud in core 16 to be a hybrid deposit. We suggest that turbidity current overspill accounts for the higher sedimentation rate, while bottom current can provide more nutrients, and also keep the fines in a turbidity current in suspension. Prolonged settling of suspension cloud would be a process similar to hemiturbidite identified by Stow and Wetzel (1990), facilitating continuous bioturbation with sedimentation.

5.2 Temporal relationships between fine-grained sedimentary facies

The temporal evolution of major sedimentary facies shows a variable depositional pattern (Fig. 8). Turbidites and hybrid deposits occurred during LGM, and turbidites were maintained until the YD at core 37. Contourites accumulated where the deposition was not dominated or disrupted by turbidity currents. The appearance of sandy contourites during YD can be well correlated between cores, except at core site 15 where erosion or non-deposition prevailed. After YD, muddy contourites contributed to Holocene deposition at a regional scale, only becoming siltier upslope in water depths of less than 800 m.

5.3 Sediment sources

Two main sediment transport pathways are expected: downslope cross-shelf supply and alongslope transport by the Labrador Current. To better trace the sediment supply from the Labrador Current, two previously studied cores providing typical signals were adopted: core 96018-06 (YD interval, hereafter 06, Li and Piper, 2015) in Flemish Pass and core 87007-07 (hereafter 07, Piper and DeWolfe, 2003) located on the upper slope of the Tail of the Banks (Fig. 1A). Core preservation was insufficient for pXRF analysis of the Holocene and YD intervals in core 07. Considering that ice was remote from the Tail of the Banks at the LGM, meltwater-related downslope sediment supply was inferred to be minor. The pXRF records in core 07 at 170-250 cm and 310-410 cm (LGM-deglaciation) are used to detect possible changes in the alongslope supply from upstream. In the study area, shelf-crossing supply carried by meltwater was largely determined by the ice position during LGM, and may therefore have been varying through time. The YD turbidite sequence is considered a better candidate for providing imprints of local Grand Banks source. Data from cores 35 (YD sandy contourites) and 37 (YD turbidites including sedimentation between events and Holocene muddy contourites) were thus plotted for comparison (Fig. 9).

Elements that are reliably measured by pXRF were selected for bivariate plots, following the procedures established by Tang and Piper (2020) in which provenance significance can be shown by a consistent ratio of two elements. The biplots between K, Ti, Zr, and Ca all indicate two main ratios (Fig. 9), except where biogenic contributions to Holocene muddy contourites (core 37) have produced higher calcite that increased Ca abundance (Fig. 9B and D). In all biplots, the Holocene in core 37, YD in core 06 and the major part of LGM in core 07 are consistently of the same ratio, interpreted as a typical signal of alongslope supply. Some data from YD intervals in cores 37 and 35 are also scattered within that ratio, but most data show a different trend in the biplots of Zr vs. Ca, Zr vs. Ti and Ca vs. Ti (Fig. 9B, C, and D), which provide evidence of down-slope transport from a different source, interpreted as the Grand Banks. The two sources overlap in the behavior of K with respect to Ti (Fig. 9A), giving difficulty to differentiate the two using these elements alone. Overall, the existence of two sources indicates that YD turbidites in core 37 were most likely to be have been fed by storminess that entrained local shelf materials, while sedimentation between turbidites still received alongslope supply. Both sources, through direct downslope flux and alongslope transport in the LC with upstream erosion of the seafloor and/or resuspension, combine to provide the sediment budget for YD sandy contourites in core 35.

5.4 Controlling factors

5.4.1 Sediment dynamic of turbidity currents

From just after H2 to ~15 ka, core 2031, located at 390 m above Narwhal Canyon floor, contains a sedimentation record of typical turbidites, giving an extremely high sedimentation rate (>900 cm/ka in the sandy interval and >400 cm/ka in the silty interval). Deposits from most of core 16 below H1, located at an inter-canyon ridge, are also interpreted to be the spillover from turbidity currents. In both canyons, turbidity currents were active at least throughout the LGM. At ~25 ka BP, local advance of the LIS across Whale Bank did not reach the SW Grand Banks shelf edge (Fig. 1A), and the ~80 km between the probable ice margin and the canyon heads prevented direct glacigenic sediment supply from the ice. Fluvioglacial meltwater across the emergent Grand Banks could carry large quantities of sediment from the ice sheet (Alley et al., 1997), known to have a critical role in supplying sediment for turbidity currents (e.g., Toucanne et al., 2008, 2012; Bernhardt et al., 2017). Fluvioglacial meltwater can lead to plunging hyperpycnal flows when sediment concentration in meltwater exceeds the density of the seawater (Piper and Normark, 2009), which can cause erosion at the shelf break as observed within DesBarres Canyon (Fig. 1B). Turbidity currents can also be triggered by settling of sediment suspended in surface plumes (Parsons et al., 2001; Hizzett et al., 2018), and slope failures from rapid sediment accumulation can generate submarine landslides that can evolve into turbidity currents without major external triggers (Girardclos et al., 2007; Bailey et al., 2021). Moreover, the sea-level lowstand coincident with the LGM likely favored triggering of turbidity currents by storms. We suggest that during LGM the canyons were fed by sediment derived from meltwater-driven processes and the remobilization of sediment.

From ~18 to 15 ka BP, successive sand-dominated turbidites were only found in core 2031 adjacent to Narwhal canyon. While the silty material tended to be transferred by fluvioglacial meltwater throughout LGM, the much sandier materials at this time were likely entrained by longshore drift from coastal erosion, suggesting meltwater was no longer able to deliver sediment to feed the canyon by 18 ka BP, at a time when the closest ice margin had retreated to close to the modern shoreline (Fig. 1A) and was ~ 200 km away from the canyon head (Fig. 8). On the Scotian margin, where the supply of glaciofluvial sediment was no longer possible after ~16 ka BP, the distance between the ice margin and canyon heads was only ~ 50 km at the maximum (Normandeau and Campbell, 2020). Around 18 ka BP, melting ice retreated across the Avalon Channel (Fig. 1A), which later likely trapped the meltwater and restricted its passageway, indicating that the availability of meltwater reaching canyon heads was mainly controlled by topography on the shelf rather than the distance from the ice margin.

Only in core 37 were turbidites found during YD, which resulted from frequent storms similar to Toomey et al. (2017) and southwestward transport of sand across the Grand Banks (Li et al., 2017). This is also evidenced by its distinct characteristics in sediment source compared to that from alongslope supply (Fig. 9). In core 2031, the absence of any stratigraphic layer correlative to turbidites in core 37 indicates turbidity currents either died out in the channel before reaching core 2031 or flows were not thick enough to over-top the levee where core 2031 is located.

5.4.2 The role of bottom currents

Grayish-red beds, interpreted as equivalent layers of red beds in cores 62 and 59 (Mao et al., 2014) and cores 42 and 48 (Rashid et al., 2019) at upstream areas, were clearly identified on the SW Grand Banks slope. The a* peaks are clearer in cores 34 and 15, but correlatable to cores 37, 16 and 35 (Fig. 6). Red sediments were sourced from the expansion of the LIS eroding Upper Paleozoic red sandstones and shales on NE Newfoundland Shelf during MIS 2 (Tripsanas and Piper, 2008), transported to the shelf edge by ice streams in conduits like Trinity Trough, Notre Dame Channel and Hawke Saddle. However, the lack of troughs with ice-streams between Trinity Trough and Haddock Channel hindered direct red sediment supply to the Grand Banks (Fig. 1A). The alongslope-flowing Labrador Current would have entrained and transported reddish sediments, along with floating calved icebergs, mixing with local Grand Banks grey sediment source and accounting for widespread reddish sediments around the Grand Banks. Deposition of grayish-red beds thus occured in the same manner as H-layers, both of which reflect current effects.

Locally, the LC interacts with episodic sediment gravity flows, forming hybrid turbidite-contourite beds at the inter-canyon ridge. The persistent current effect is also revealed by the configuration of a more pronounced sediment levee on the north-western side of the DesBarres Canyon. The Coriolis force may have affected turbidity currents flowing southwest along the canyon, which resulted in enhanced erosion, as a larger edge gradient is observed at the northwest levee (Fig. 1B). However, direct overspill of turbidity currents from DesBarres Canyon was likely prevented by the height of the canyon wall (> 400 m), thus the Coriolis force did not create great differences in levee height. We suggest that the bottom current should have exerted an important impact, with its ability to capture and redistribute suspended fines from the upper dilute layer of turbidity current, forming asymmetric levees from this simultaneous interaction. Similar hybrid turbidite-contourite beds have also been revealed by other studies (Michels et al., 2002; Mencaroni et al., 2021).

5.4.3 Additional sediment influx from melting icebergs

IRDs are widespread, except in turbidites where the sedimentation rate is high and deposition is rapid. IRD are a major component constructing glacial contourite depositional system), mostly evidenced by uniform-sized IRD granules at cm scale, which are parallel to the millimetre-scale laminae (Fig. 10a). This interplay between current sorting and sediment input from ice-rafting is also observed on other glaciated margins, e.g., on the Antarctic Peninsula margin (Lucchi et al., 2002) and western Barents Sea shelf (Lucchi et al., 2013; Lantzsch et al., 2017).

In particular, core 15 has the greatest thickness between H1 and H2, contrasting to its condensed section before H2 and after H1. Most of this thick interval consists of grayish-red mud (~1.9 m). Its reddish colour indicates the same source as grayish-red beds in core 34, 35 and also red beds recognized in other cores on the SE Grand Banks slope (Rashid et al., 2019). Reddish sediments were provided to the Grand Banks margin either from iceberg calving or in meltwater plumes from ice streams occupying troughs, both of which would be entrained and transported by the along-slope current. Grain-size in grayish-red mud in core 15 show less current-sorting compared to time-equivalent sediment elsewhere (510-578 in core 34 and 625-690 in core 35), revealing the current sorting was unable to keep pace with sediment input, in line with its high sedimentation rate. We interpret the grayish-red mud as episodes of sediments dumping from iceberg rollover, representing rapid sediment deposition events related to iceberg rafting from the NE Newfoundland Shelf, based on 1) *Chondrites*-like burrows at 432-455 cm (Fig. 10a), known to be indicative of rapidly accumulating muds tolerant to low oxygen conditions (Wetzel et al., 2008; Dorador et al., 2021); 2) higher contents of stratified angular outsized pebbles and randomly distributed clasts (Fig. 10b and c); 3) layers of accumulated fine sand with IRD, all similar to Vermassen et al. (2019); 4) foraminifers are sparse (<1%) in sand fraction, implying the presence of a freshwater cap and/or rapid deposition.

5.5 Sedimentary model for depositional systems

We propose two models based on the distribution of sedimentary products through time

(Fig. 11). From LGM to early deglaciation, there was sufficient downslope sediment supply (① in Fig. 11a), contributing to the formation of turbidity currents. However, sands were preferentially trapped within canyon heads, restricting the distribution of turbidites (② in Fig. 11a). Suspended fines from intermittent turbidity currents likely formed a low-density cloud above a certain height (③ in Fig. 11a), which subsequently was captured by the alongslope current (④ in Fig. 11a), yielding mixed deposits found on the inter-canyon ridge. The short lateral diversion by the alongslope current is indicated by the asymmetric levees of the canyon (Fig. 1B), but that material was not transported a longer-distance downstream outside the canyon. Therefore, the normal slope outside of canyons was sheltered from turbidity currents, and a glacial contourite depositional system was able to develop (⑤ in Fig. 11a) with additional sediment supply from icebergs (⑥ in Fig. 11a). As a consequence, an irregular depositional pattern prevailed at this time, demonstrating the spatial difference in sedimentary processes. By the Holocene, ice retreated to the present distant coastline and eventually melted completely. In contrast to the glacially influenced period, down-slope processes are of minor importance.-Along-slope processes became predominant, contributing to an overall homogeneous sedimentation, where deposition was dominated by muddy contourites that become siltier upslope. Along the course of the current, sedimentation rates may be lower beneath the axis of current and higher in the low velocity zones upslope and downslope. The axis is likely at 1200-1350 m water depth where the lowest sedimentation rates were found (cores 15 and 16), which is consistent with the structure of the flow field in the Newfoundland Basin investigated by Mertens et al. (2014). Sedimentation rates increase towards shallower (core 34) and deeper (cores 2031 and 37) water depths (Fig. 3). However, variations in sedimentation thickness present in cores 16 and 35, both located in a similar water depth, indicate that there are other controlling factors rather than solely the overall current regime. Holocene sedimentation thickness varies geographically, being thicker near Narwhal Canyon, intermediate southeast of DesBarres Canyon, and thinnest northwest of the main thalweg of DesBarres Canyon. This broad trend is consistent with the fact that along-slope current velocity can be directly affected by changes in topography inherited from the

LGM along its course (Stow et al., 2008). Compared to the current condition over a normal smooth slope (e.g., southeast of DesBarres Canyon), the deep DesBarres Canyon would allow flow expansion of the current (① in Fig. 11b) and could shed mesoscale eddies affecting the shallower inter-ridge and overbank core sites to the northwest (Faugères and Stow, 2008). An analogous process at Narwhal Canyon would account for the variable current velocity inferred from core 2031 and 37 at a similar water depth. This is in agreement with different sedimentation rates among cores in Halibut Canyon to the northwest (unit 3 of Holocene age in Tang and Piper, 2020). Northwest of DesBarres Canyon, the much higher outer levee formed at LGM presents an obstacle, restricting the impinging flow. This may result in local acceleration and hampers deposition (② in Fig. 11b), creating the lowest sedimentation rate. We conclude that Holocene deposition is mainly a process of muddy drift building, with spatial deposition pattern being mainly controlled by an along-slope current interacting with pre-existing morphology.

6. Conclusions

This study used the analysis of sediment cores to understand a deep-water depositional system since the Late Pleistocene on the glacially influenced SW Grand Banks Slope off Newfoundland. The results present the spatial and temporal facies distribution, demonstrating an irregular depositional evolution. The main conclusions are:

1) Outsized IRD that preferentially accumulated within laminae are well-aligned, with their long axes roughly parallel to the wavy-parallel bedding in the silty contourites, constituting the traction structure in the silty contourites. IRD are better sorted, notable in their uniform size, which is the clear imprint of current sorting that has been hardly detected on margins without glacial influence.

2) YD is characterized by the development of sandy contourites, as a result of intensified LC strength and cross-shelf supply of coarse sediments by storms. It can be distinguished from overlying mud-dominated sediment in the Holocene, and can be well correlated across the region.

3) Downslope turbidity currents, alongslope bottom currents and additional sediment

input from melting icebergs are the three key processes building the SW Grand Banks slope. Sand was preferentially deposited within canyon heads, so turbidites are restricted to canyons. Contourites are distributed on the slope, and hybrid deposits are found on inter-canyon ridges.

4) Topography on the shelf determines the pathway of meltwater, controlling the availability of meltwater discharge reaching canyon heads. At LGM, the LIS did not cross the SW Grand Banks shelf but was within 80 km of the canyon heads. Fluvioglacial meltwater was able to deliver sufficient sediments to the slope at least until early deglaciation at around 18 ka. After that, the main trigger of turbidity currents was oceanographically controlled. Turbidity currents almost ceased after the Younger Dryas, leaving Holocene deposition a process of drift-building led by the alongslope current.

Data availability

Grainsize data are available at: https://ed.gdr.nrcan.gc.ca/grainsize_e.php.

Radiocarbon dates can be found at: https://ed.gdr.nrcan.gc.ca/radiocarbon_e.php.

Other data used in this paper are managed at Geological Survey of Canada (Atlantic) and can only be accessed with an approved request from the data curator. Interested readers should make a request or contact the corresponding author for assistance.

Acknowledgements

The study was supported by the Fundamental Research Funds for National Universities, China University of Geosciences (Wuhan) and the Research Fund Program of Guangdong Provincial Key Laboratory of Marine Resources and Coastal Engineering. Laboratory work was supported by the Geological Survey of Canada, Marine Geoscience for Marine Spatial Planning program and a Natural Sciences and Engineering Research Council Discovery Grant (04217-2016) to DJWP. We thank Owen Brown, Jenna Higgins and Kate Jarrett for facilitating lab work. Constructive reviews by three reviewers improved the quality of this paper.

References

Alley, R.B., Cuffey, K., Evenson, E., Strasser, J., Lawson, D., Larson, G., 1997. How glaciers entrain and transport basal sediment: physical constraints. Quaternary Science Reviews 16, 1017–1038.

Andrews, J., Tedesco, K., 1992. Detrital carbonate-rich sediments, northwestern Labrador Sea: Implications for ice-sheet dynamics and iceberg rafting (Heinrich) events in the North Atlantic. Geology 20, 1087–1090.

Andrews, J. T., 2000. Icebergs and iceberg rafted detritus (IRD) in the North Atlantic: facts and assumptions. Oceanography, 13(3), 100–108.

Andrews, J. T., Jennings, A. E., Kerwin, M., Kirby, M., Manley, W., Miller, G. H., Bond, G., and MacLean, B., 1995. A Heinrich-like event, H-0 (DC-0): Source(s) for detrital carbonate in the North Atlantic during the Younger Dryas Chronozone, Paleoceanography, 10, 943–952.

Andrews, J.T., Voelker, A.H., 2018. "Heinrich events" (& sediments): A history of terminology and recommendations for future usage. Quaternary Science Reviews 187, 31–40.

Bailey, L.P., Clare, M.A., Rosenberger, K.J., Cartigny, M.J., Talling, P.J., Paull, C.K., Gwiazda, R., Parsons, D.R., Simmons, S.M., Xu, J., 2021. Preconditioning by sediment accumulation can produce powerful turbidity currents without major external triggers. Earth and Planetary Science Letters 562, 116845.

Barnett-Moore, N., Müller, D.R., Williams, S., Skogseid, J., Seton, M., 2018. A reconstruction of the North Atlantic since the earliest Jurassic. Basin Research 30, 160–185.

Bernhardt, A., Schwanghart, W., Hebbeln, D., Stuut, J.-B.W., Strecker, M.R., 2017. Immediate propagation of deglacial environmental change to deep-marine turbidite systems along the Chile convergent margin. Earth and Planetary Science Letters 473, 190–204.

Bonifay, D., Piper, D.J.W., 1988. Probable Late Wisconsinan ice margin on the upper continental slope off St. Pierre Bank, eastern Canada. Canadian Journal of Earth Sciences 25, 853–865.

Boyd, R., Scott, D.B., Douma, M., 1988. Glacial tunnel valleys and Quaternary history of the outer Scotian shelf. Nature 333, 61-64.

Bozzano, G., Violante, R.A., Cerredo, M.E., 2011. Middle slope contourite deposits and associated sedimentary facies off NE Argentina. Geo-Marine Letters 31, 495–507.

Cameron, G.D.M., King, E.L., 2011. Possible flood events in large shelf crossing troughs on the Southeast Canadian Margin; Geological Survey of Canada, Open File 6995.

Chough, S., Lee, G., Park, B., Kim, S., 1984. Fine structures of turbidite and associated muds in the Ulleung (Tsushima) Basin, East Sea (Sea of Japan). Journal of Sedimentary Research 54, 1212–1220.

Cochonat, P., Ollier, G., Michel, J., 1989. Evidence for slope instability and current-induced sediment transport, the RMS Titanic wreck search area, Newfoundland rise. Geo-marine Letters 9, 145–152.

Dalton, A.S., Margold, M., Stokes, C.R., Tarasov, L., Dyke, A.S., and 66 others, 2020. An updated radiocarbon-based ice margin chronology for the last deglaciation of the North American Ice Sheet Complex. Quaternary Science Reviews 234, 106223.

Dalton, A.S., Stokes, C.R., Batchelor, C.L., 2022. Evolution of the Laurentide and Innuitian ice sheets prior to the Last Glacial Maximum (115 ka to 25 ka). Earth-Science Reviews 224, 103875.

Dorador, J., Rodríguez-Tovar, F.J., Mena, A., Francés, G., 2019. Lateral variability of ichnological content in muddy contourites: Weak bottom currents affecting organisms' behavior. Scientific reports 9, 1–7.

Dorador, J., Rodríguez-Tovar, F.J., Mena, A., Francés, G., 2021. Deep-sea bottom currents influencing tracemaker community: An ichnological study from the NW Iberian margin. Marine Geology 437, 106503.

Ellwood, B.B., Ledbetter, M.T., 1977. Antarctic bottom water fluctuations in the Vema Channel: effects of velocity changes on particle alignment and size. Earth and Planetary

Science Letters 35, 189–198.

Faugères, J.-C., Gonthier, E., Stow, D.A., 1984. Contourite drift molded by deep Mediterranean outflow. Geology 12, 296–300.

Faugères, J.-C., Stow, D., 2008. Contourite drifts: nature, evolution and controls. Developments in Sedimentology 60, 257–288.

Fleming, K. M., Johnston, P., Zwartz, D., Yokoyama, Y., Lambeck, K., Chappell, J., 1998. Refining the eustatic sea-level curve since the Last Glacial Maximum using far- and intermediate-field sites. Earth and Planetary Science Letters 163, 327–342.

Folk, R.L., Ward, W.C., 1957. Brazos River bar [Texas]; a study in the significance of grain size parameters. Journal of Sedimentary Petrology 27, 3–26.

Fratantoni, P.S., McCartney, M.S., 2010. Freshwater export from the Labrador Current to the North Atlantic Current at the Tail of the Grand Banks of Newfoundland. Deep Sea Research Part I: Oceanographic Research Papers 57, 258–283.Gauley, B.J.L., 2001. Lithostratigraphy and sediment failure on the central Scotian Slope (Master dissertation). Dalhousie University, Halifax, Canada.

Girardclos, S., Schmidt, O.T., Sturm, M., Ariztegui, D., Pugin, A., Anselmetti, F.S., 2007. The 1996 AD delta collapse and large turbidite in Lake Brienz. Marine Geology 241, 137–154.

Grant, A., McAlpine, K., 1990. The continental margin around Newfoundland. In: M.J. Keen and G.L.Williams. (Eds.), Geology of the Continental Margin of Eastern Canada (Chap. 6). Geological Society of America, Geology of Canada 2, 239–292.

Han, G., Lu, Z., Wang, Z., Helbig, J., Chen, N., De Young, B., 2008. Seasonal variability of the Labrador Current and shelf circulation off Newfoundland. Journal of Geophysical Research: Oceans 113, C10013.

Heaton, T.J., Köhler, P., Butzin, M., Bard, E., Reimer, R.W., Austin, W.E., Ramsey, C.B., Grootes, P.M., Hughen, K.A., Kromer, B., 2020. Marine20—the marine radiocarbon age calibration curve (0–55,000 cal BP). Radiocarbon 62, 779–820.

Heinrich, H., 1988. Origin and consequences of cyclic ice rafting in the northeast Atlantic

Ocean during the past 130,000 years. Quaternary Research 29, 142–152.

Hemming, S.R., 2004. Heinrich events: Massive late Pleistocene detritus layers of the North Atlantic and their global climate imprint. Reviews of Geophysics 42, RG1005.

Hennekam, R., de Lange, G., 2012. X-ray fluorescence core scanning of wet marine sediments: methods to improve quality and reproducibility of high-resolution paleoenvironmental records. Limnol. Oceanogr. Methods 10 (12), 991–1003.

Hesse, R., Khodabakhsh, S., 1998. Depositional facies of late Pleistocene Heinrich events in the Labrador Sea. Geology 26, 103–106.

Hesse, R., Khodabakhsh, S., Klaucke, I., Ryan, W.B., 1997. Asymmetrical turbid surface-plume deposition near ice-outlets of the Pleistocene Laurentide ice sheet in the Labrador Sea. Geo-Marine Letters 17, 179–187.

Hizzett, J.L., Hughes Clarke, J.E., Sumner, E.J., Cartigny, M., Talling, P., Clare, M., 2018. Which triggers produce the most erosive, frequent, and longest runout turbidity currents on deltas? Geophysical Research Letters 45, 855–863.

Hundert, T., Piper, D.J.W., 2008. Late Quaternary sedimentation on the southwestern Scotian Slope, eastern Canada: relationship to glaciation. Canadian Journal of Earth Sciences 45, 267–285.

Jenner, K., Campbell, D., Piper, D.J.W., 2018. Along-slope variations in sediment lithofacies and depositional processes since the Last Glacial Maximum on the northeast Baffin margin, Canada. Marine Geology 405, 92–107.

Lantzsch, H., Hanebuth, T.J., Horry, J., Grave, M., Rebesco, M., Schwenk, T., 2017. Deglacial to Holocene history of ice-sheet retreat and bottom current strength on the western Barents Sea shelf. Quaternary Science Reviews 173, 40–57.Li, G., Piper, D.J.W., 2015. The influence of meltwater on the Labrador Current in Heinrich event 1 and the Younger Dryas. Quaternary Science Reviews 107, 129–137.

Li, M.Z., Wu, Y., Han, G., Prescott, R.H., Tang, C.C., 2017. A modeling study of the impact of major storms on seabed shear stress and sediment transport on the Grand Banks of Newfoundland. Journal of Geophysical Research: Oceans 122, 4183–4216.

Li, M.Z., Wu, Y., Prescott, R.H., Tang, C.C., Han, G., 2015. A modeling study of the impact of major storms on waves, surface and near-bed currents on the Grand Banks of Newfoundland. Journal of Geophysical Research: Oceans 120, 5358–5386.

Liverman, D., 1994. Relative sea-level history and isostatic rebound in Newfoundland, Canada. Boreas. 23. 217–230.

Lowe, J.J., Rasmussen, S.O., Björck, S., Hoek, W.Z., Steffensen, J.P., Walker, M.J., Yu, Z., Intimate Group, 2008. Synchronisation of palaeoenvironmental events in the North Atlantic region during the Last Termination: a revised protocol recommended by the INTIMATE group. Quaternary Science Reviews 27, 6–17.

Lucchi, R.G., Rebesco, M., 2007. Glacial contourites on the Antarctic Peninsula margin: insight for palaeoenvironmental and palaeoclimatic conditions. Geological Society, London, Special Publications 276, 111–127.

Lucchi, R.G., Rebesco, M., Camerlenghi, A., Busetti, M., Tomadin, L., Villa, G., Persico, D., Morigi, C., Bonci, M., Giorgetti, G., 2002. Mid-late Pleistocene glacimarine sedimentary processes of a high-latitude, deep-sea sediment drift (Antarctic Peninsula Pacific margin). Marine Geology 189, 343–370.

MacRae, R.A., Christians. A.R., 2013. A reexamination of Pleistocene tunnel valley distribution on the central Scotian Shelf. Canadian Journal of Earth Sciences 50 (5), 535-544.

Mao, L., Piper, D.J.W., Saint-Ange, F., Andrews, J.T., 2018. Labrador Current fluctuation during the last glacial cycle. Marine Geology 395, 234–246.

Mao, L., Piper, D.J.W., Saint-Ange, F., Andrews, J.T., Kienast, M., 2014. Provenance of sediment in the Labrador Current: a record of hinterland glaciation over the past 125 ka. Journal of Quaternary Science 29, 650–660.

Marchitto, T.M., Broecker, W.S., 2006. Deep water mass geometry in the glacial Atlantic Ocean: A review of constraints from the paleonutrient proxy Cd/Ca. Geochemistry, Geophysics, Geosystems 7, Q12003.

Masson, D., Plets, R., Huvenne, V., Wynn, R., Bett, B., 2010. Sedimentology and depositional history of Holocene sandy contourites on the lower slope of the Faroe–Shetland Channel, northwest of the UK. Marine Geology 268, 85–96.

McCall, C., 2006. A geological and geophysical study of the 1929 Grand Banks slide (Master dissertation). Saint Mary's University, Halifax, Canada.

McCave, I., Andrews, J., 2019. Distinguishing current effects in sediments delivered to the ocean by ice. I. Principles, methods and examples. Quaternary Science Reviews 212, 92–107.

McCave, I., Hall, I.R., 2006. Size sorting in marine muds: Processes, pitfalls, and prospects for paleoflow-speed proxies. Geochemistry, Geophysics, Geosystems 7, Q10N05.

McCave, I., Manighetti, B., Robinson, S., 1995. Sortable silt and fine sediment size/composition slicing: parameters for palaeocurrent speed and palaeoceanography. Paleoceanography 10, 593–610.

McNeely, R., Dyke, A.S., Southon, J.R., 2006. Canadian marine reservoir ages, preliminary assessment. Geological Survey of Canada Open File 5049.

Mencaroni, D., Urgeles, R., Camerlenghi, A., Llopart, J., Ford, J., Sanchez Serra, C., Meservy, W., Gracia, E., Rebesco, M., Zitellini, N., 2021. A mixed turbidite–contourite system related to a major submarine canyon: The Marquês de Pombal Drift (south-west Iberian margin). Sedimentology 68, 2069–2096.

Mertens, C., Rhein, M., Walter, M., Böning, C. W., Behrens, E., Kieke, D., Steinfeldt, R., Stöber, U., 2014. Circulation and transports in the Newfoundland Basin, western subpolar North Atlantic. Journal of Geophysical Research: Oceans 119, 7772–7793.

Michels, K., Kuhn, G., Hillenbrand, C.-D., Diekmann, B., Fütterer, D.K., Grobe, H., Uenzelmann-Neben, G., 2002. The southern Weddell Sea: combined contourite-turbidite sedimentation at the southeastern margin of the Weddell Gyre. Geological Society, London, Memoirs 22, 305–323.

Miller, A.A., Fader, G.B., Moran, K., 2001. Late Wisconsinan ice advances, ice extent, and glacial regimes interpreted from seismic data, sediment physical properties, and Foraminifera: Halibut Channel, Grand Banks of Newfoundland, in: Deglacial History and Relative Sea-Level Changes, Northern New England and Adjacent Canada 351, 51–107.

Milne, G. A., Long, A. J., Bassett, S. E., 2005. Modelling Holocene relative sea-level observations from the Caribbean and South America. Quaternary Science Reviews 24, 1183–1202.

Mulder, T., Faugères, J.-C., Gonthier, E., 2008. Mixed turbidite–contourite systems. Developments in Sedimentology 60, 435–456.

Murton, J.B., Bateman, M.D., Dallimore, S.R., Teller, J.T., Yang, Z., 2010. Identification of Younger Dryas outburst flood path from Lake Agassiz to the Arctic Ocean. Nature 464, 740–743.

Nelson, C.H., Baraza, J., Maldonado, A., 1993. Mediterranean undercurrent sandy contourites, Gulf of Cadiz, Spain. Sedimentary Geology 82, 103–131.

Nishida, N., 2016. Microstructure of muddy contourites from the Gulf of Cádiz. Marine Geology 377, 110–117.

Normandeau, A., Campbell, D.C., 2020. Recurrence of turbidity currents on glaciated continental margins: A conceptual model from eastern Canada. Journal of Sedimentary Research 90, 1305–1321.

Parsons, J.D., Bush, J.W., Syvitski, J.P., 2001. Hyperpycnal plume formation from riverine outflows with small sediment concentrations. Sedimentology 48, 465–478.

Pass, D., Piper D.J.W., and Campbell D.C., 2000. Quaternary geology of the continental slope in the vicinity of the Narwhal F-99 well site; Geological Survey of Canada, Open File 3894.

Pearce, C., Seidenkrantz, M. S., Kuijpers, A., Massé, G., Reynisson, N. F., Kristiansen, S. M., 2013. Ocean lead at the termination of the Younger Dryas cold spell. Nature communications, 4, 1664.

Pearce, C., Andrews, J. T., Bouloubassi, I., Hillaire-Marcel, C., Jennings, A. E., Olsen, J., Kuijpers, A., Seidenkrantz, M.-S., 2015. Heinrich 0 on the east Canadian margin: Source, distribution, and timing, Paleoceanography, 30, 1613–1624.

Pearce, C., Seidenkrantz, M.-S., Kuijpers, A., Reynisson, N.F., 2014. A multi-proxy reconstruction of oceanographic conditions around the Younger Dryas–Holocene transition in Placentia Bay, Newfoundland. Marine Micropaleontology 112, 39–49.

Pe-Piper, G., Piper, D.J.W., Jansa, L.F., De Jonge, A., 2007. Early Cretaceous opening of the North Atlantic Ocean: Implications of the petrology and tectonic setting of the Fogo Seamounts off the SW Grand Banks, Newfoundland. Geological Society of America Bulletin 119, 712–724.

Petrie, B., Isenor, A., 1985. The near-surface circulation and exchange in the Newfoundland Grand Banks region. Atmosphere-Ocean 23, 209–227.

Piper, D.J.W., 1988. Glaciomarine sedimentation on the continental slope off eastern Canada. Geoscience Canada 15, 23–28.

Piper, D.J.W., 2005. Late Cenozoic evolution of the continental margin of eastern Canada. Norwegian Journal of Geology 85, 305–318.

Piper, D.J.W., Deptuck, M., Mosher, D.C., Clarke, J.E.H., Migeon, S., 2012. Erosional and depositional features of glacial meltwater discharges on the eastern Canadian continental margin. In Prather, B.E., Deptuck, M.E., Mohrig, D., van Hoorn, B., and Wynn, R.B. (Eds.), Applications of the Principles of Seismic Geomorphology to Continental Slope and Base-of-Slope Systems: Case Studies from Seafloor and Near-Seafloor Analogues: Society for Sedimentary Geology (SEPM) Special Publication 99, 61–80.

Piper, D.J.W., Gould, K., 2004. Late Quaternary geological history of the continental slope, South Whale Subbasin, and implications for hydrocarbon development, southwestern Grand Banks of Newfoundland. Geological Survey of Canada, Current Research D-1.

Piper, D.J.W., Lawrence, T., Gould, K., 2006. Report on cores 2004-024 15 and 16, DesBarres Canyon area, SW Grand Banks; Geological Survey of Canada, Open File 5118.

Piper, D.J.W., Li, G., Andrews, J.T., Jennings, A.E., Robertson, L., 2021. Transport of fine-grained sediment in oceanic currents: Holocene supply to sediment drifts around Flemish Cap by the Labrador Current. Marine Geology 436, 106494.

Piper, D.J.W., Macdonald, A., 2001. Timing and position of Late Wisconsinan ice-margins on the upper slope seaward of Laurentian Channel. Géographie physique et Quaternaire 55, 131–140.

Piper, D.J.W., Normark, W.R., 2009. Processes that initiate turbidity currents and their influence on turbidites: a marine geology perspective. Journal of Sedimentary Research 79, 347–362.

Piper, D.J.W., Skene, K.I., Morash, N., 1999. History of major debris flows on the Scotian Rise, offshore Nova Scotia. Geological Survey of Canada, Current Research 203–212.

Piper, D.J.W., 1978. Turbidite muds and silts on deep-sea fans and abyssal plains. In: Stanley, D.J., Kelling, G (Editors), Sedimentation in Submarine Canyons, Fans and Trenches. Dowden, Hutchinson and Ross, Stroudsburg, Pennsylvania, 163–176.

Rashid, H., Piper, D.J.W., Flower, B.P., 2011. The meltwater signal of Younger Dryas: a new assessment from the Labrador Sea and northwest Atlantic Ocean. In: Abrupt Climate Change: Mechanisms, Patterns, and Impacts; AGU Geophysical Monograph Series 193, 93B110.

Rashid, H., Piper, D.J.W., MacKillop, K., Ouellette, D., Vermooten, M., Muñoz, A., Jiménez, P., 2019. Dynamics of sediments on a glacially influenced, sediment starved, current-swept continental margin: The SE Grand Banks Slope off Newfoundland. Marine Geology 408, 67–86.

Rashid, H., Piper, D. J. W., Lazar, K. B., McDonald, K., Saint-Ange, F., 2017. The Holocene Labrador Current: Changing linkages to atmospheric and oceanographic forcing factors, Paleoceanography, 32, 498– 510.

Rasmussen, S.O., Andersen, K.K., Svensson, A., Steffensen, J.P., Vinther, B.M., Clausen, H.B., Siggaard-Andersen, M., Johnsen, S.J., Larsen, L.B., Dahl-Jensen, D., 2006. A new Greenland ice core chronology for the last glacial termination. Journal of Geophysical Research: Atmospheres 111, D06102.

Rebesco, M., Hernández-Molina, F.J., Van Rooij, D., Wåhlin, A., 2014. Contourites and associated sediments controlled by deep-water circulation processes: State-of-the-art and future considerations. Marine Geology 352, 111–154.

Roger, J., Saint-Ange, F., Lajeunesse, P., Duchesne, M.J., St-Onge, G., 2013. Late Quaternary glacial history and meltwater discharges along the Northeastern Newfoundland Shelf. Canadian Journal of Earth Sciences 50, 1178–1194.

Shaw, J., Piper, D.J.W., Fader, G., King, E., Todd, B., Bell, T., Batterson, M., Liverman, D., 2006. A conceptual model of the deglaciation of Atlantic Canada. Quaternary Science Reviews 25, 2059–2081.

Skene, K.I., Piper, D.J.W., 2003. Late Quaternary stratigraphy of Laurentian Fan: a record of events off the eastern Canadian continental margin during the last deglacial period. Quaternary International 99, 135–152.

Stow, D., Faugères, J.-C., 2008. Contourite facies and the facies model. Developments in Sedimentology 60, 223–256.

Stow, D., Hernández-Molina, F., Llave, E., Bruno, M., García, M., del Rio, V.D., Somoza, L., Brackenridge, R., 2013. The Cadiz Contourite Channel: Sandy contourites, bedforms and dynamic current interaction. Marine Geology 343, 99–114.

Stow, D., Hunter, S., Wilkinson, D., Hernández-Molina, F., 2008. The nature of contourite deposition. Developments in Sedimentology 60, 143–156.

Stow, D., Smillie, Z., 2020. Distinguishing between deep-water sediment facies: Turbidites, contourites and hemipelagites. Geosciences 10, 68.

Stow, D.A., Faugères, J.-C., Howe, J.A., Pudsey, C.J., Viana, A.R., 2002. Bottom currents, contourites and deep-sea sediment drifts: current state-of-the-art. Geological Society, London, Memoirs 22, 7–20.

Stow, D.A., Wetzel, A., 1990. Hemiturbidite: a new type of deep-water sediment. Presented at the Proceedings of the Ocean Drilling Program, Scientific Results, Ocean Drilling Program College Station TX, 25–34.

Stuiver, M., Reimer, P.J., 1993. Extended ^{14}C data base and revised CALIB 3.0 ^{14}C age calibration program. Radiocarbon 35, 215–230.

Tang, M., Piper, D.J.W., 2020. Down-canyon evolution of turbidity currents at a late-glacial ice margin: Halibut Canyon, offshore southeastern Canada. Marine Geology 424, 106182.

Toomey, M.R., Korty, R.L., Donnelly, J.P., van Hengstum, P.J., Curry, W.B., 2017. Increased hurricane frequency near Florida during Younger Dryas Atlantic meridional overturning circulation slowdown. Geology 45, 1047–1050.

Toucanne, S., Zaragosi, S., Bourillet, J.-F., Dennielou, B., Jorry, S.J., Jouet, G., Cremer, M., 2012. External controls on turbidite sedimentation on the glacially-influenced Armorican margin (Bay of Biscay, western European margin). Marine Geology 303, 137–153.

Toucanne, S., Zaragosi, S., Bourillet, J.-F., Naughton, F., Cremer, M., Eynaud, F., Dennielou, B., 2008. Activity of the turbidite levees of the Celtic–Armorican margin (Bay of Biscay) during the last 30,000 years: imprints of the last European deglaciation and Heinrich events. Marine Geology 247, 84–103.

Tripsanas, E.K., Piper, D.J.W., 2008. Late Quaternary stratigraphy and sedimentology of Orphan Basin: Implications for meltwater dispersal in the southern Labrador Sea. Palaeogeography, Palaeoclimatology, Palaeoecology 260, 521–539.

Tripsanas, E.K., Piper, D.J.W., Campbell, D.C., 2008. Evolution and depositional structure of earthquake-induced mass movements and gravity flows: Southwest Orphan Basin, Labrador Sea. Marine and Petroleum Geology 25, 645–662.

Vermassen, F., Wangner, D.J., Dyke, L.M., Schmidt, S., Cordua, A.E., Kjær, K.H., Haubner, K., Andresen, C.S., 2019. Evaluating ice-rafted debris as a proxy for glacier calving in Upernavik Isfjord, NW Greenland. Journal of Quaternary Science 34, 258–267.

Wade, J., MacLean, B., 1990. The geology of the southeastern margin of Canada. In: Keen, M.J., Williams, G.L. (Eds.), Geology of the Continental Margin off Eastern Canada. Geological Survey of Canada, Geology of Canada 2, 190–238.

Wang, D., Hesse, R., 1996. Continental slope sedimentation adjacent to an ice-margin. II. Glaciomarine depositional facies on Labrador Slope and glacial cycles. Marine Geology 135, 65–96.

Wang, Z., Brickman, D., Greenan, B.J., 2019. Characteristic evolution of the Atlantic

Meridional Overturning Circulation from 1990 to 2015: An eddy-resolving ocean model study. Deep Sea Research Part I: Oceanographic Research Papers 149, 103056.

Wetzel, A., Werner, F., Stow, D., 2008. Chapter 11 Bioturbation and biogenic sedimentary structures. Contourites. Developments in Sedimentology 60, 183–202.

Table captions

Table 1: Cores used in this study.

Table 2: ^{14}C-AMS dates used in the study. Radiocarbon dates were converted to calibrated years BP using Calib 8.1 and the Marine 20 calibration curve of Heaton et al. (2020) with a ΔR of 144 ± 35.

Table S1: ^{14}C-AMS dates shown on the seismic profiles in supplementary figures. Radiocarbon dates were converted to calibrated years BP using Calib 8.1 and the Marine 20 calibration curve of Heaton et al. (2020) with a ΔR of 60 ± 40 for cores at Western Bank, Scotian margin and ΔR 144 ± 38 for all others.

Figure captions

Figure 1: **(A)** Map showing major physiographic features around the Grand Banks of Newfoundland, location of the study area, principal flow paths of the along-slope currents, ice margins (18.7 ka and 26 ka) modified from Dalton et al. (2020, 2022) and other cores discussed in the text. (All ages are calibrated) (**B**) Bathymetric map (extrapolated from the GEBCO gridded bathymetry data) of the study area, showing location of sediment cores used in this study.

Figure 2. Summary of lithofacies 1-4 associated with sedimentary features and frequency plots of grain size from selected examples.

Figure 3: Summary of lithofacies 5-8 associated with sedimentary features and frequency plots of grain size from selected examples.

Figure 4: Lithofacies, high-resolution images, X- radiographs, grain size distribution curve, bulk density and elemental ratios of core 34.

Figure 5: Lithofacies, high-resolution images, X- radiographs, grain size distribution curve, bulk density and elemental ratios of core 37. *Zoophycos* are marked by orange arrows on X- radiographs.

Figure 6: Lithostratigraphic summary of cores 2031, 37, 15, 16, 35 and 34 with calibrated radiocarbon ages, downcore plots of pXRF Ca/Ti ratios and a*. The correlated horizons in dotted orange lines show the base of Younger Dryas, Heinrich 1 and 2. Note core 2031 has a different depth scale (to left). WD = Water depth; TWC = Trigger weight core; GR = Grayish-red bed.

Figure 7: Facies associations of sandy contourites with grain-size density curves, showing a bi-gradational sequence that is coarsening upward from muddy through bioturbated silty mud to structureless sandy mud, and then fining through mottled silt back to muddy deposits. Downcore plots of bulk density and element ratios are plotted against the depth.

Figure 8: Temporal occurrence of interpreted fine-grained sedimentary facies, relative sea-level history based on data from Fleming et al. (1998), and Milne et al. (2005), and the distance from ice margin to the canyon heads measured from Dalton et al. (2020, 2022).

Figure 9: Biplots of selected elements (pXRF) to investigate provenance of sedimentary facies. **(A)** K vs. Ti, **(B)** Zr vs. Ca, **(C)** Zr vs. Ti, **(D)** Ca vs. Ti. Cross-shelf supply and alongslope supply indicated by constantly different ratios are circled in green and pink, respectively. Intervals with biogenic contributions increasing Ca abundance form an additional group out of the trend of both ratios.

Figure 10: Typical sedimentary features of the thick grayish-red bed in core 15, illustrated by X- radiograph. Bar segments are 1 cm.

Figure 11: Conceptual models for periods of **(a)** LGM to the early deglaciation and **(b)** the Holocene, presenting the depositional processes and background of the SW Grand Banks Slope off Newfoundland.

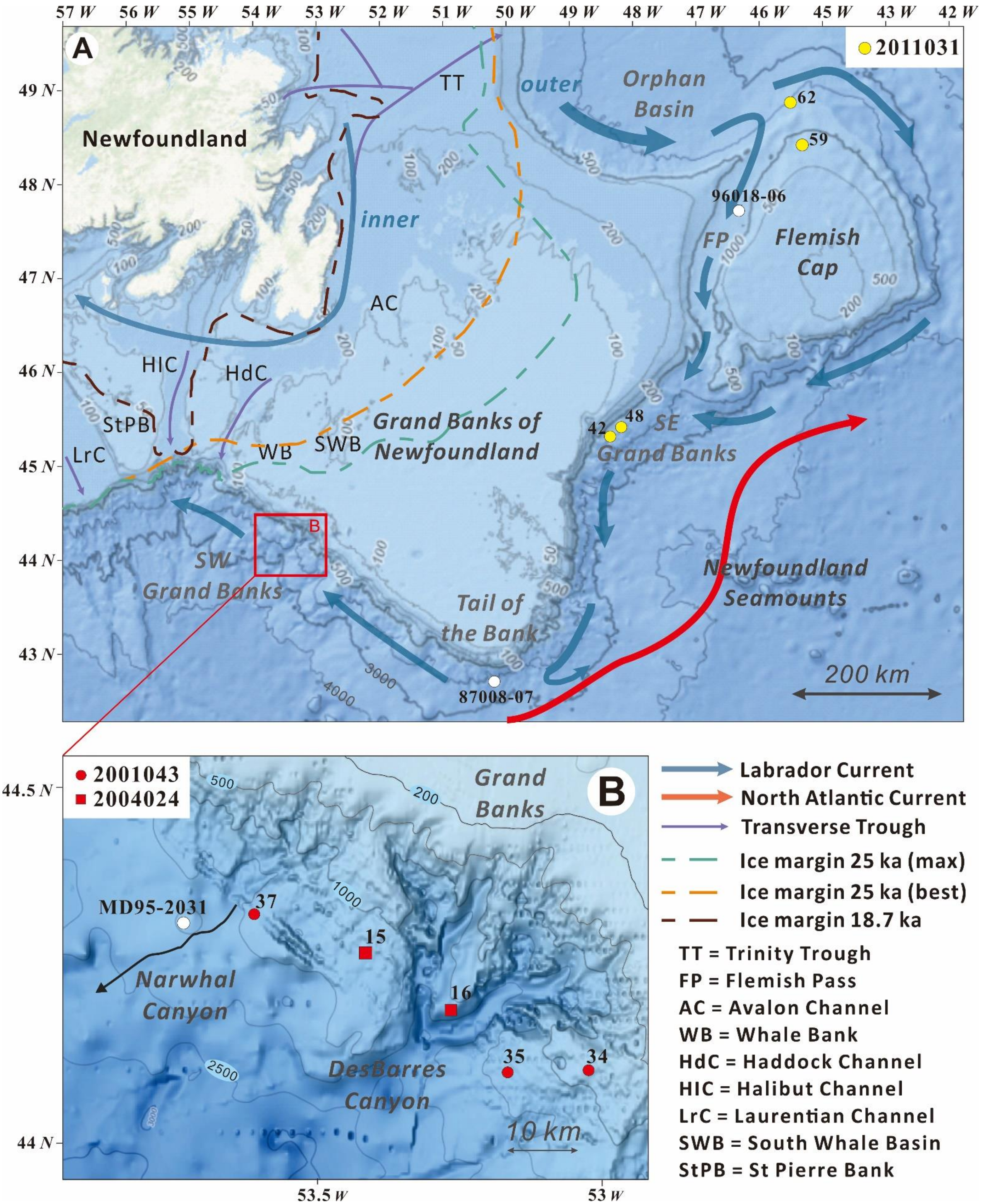

A
2011031
Newfoundland
Orphan Basin
outer
inner
TT
AC
Flemish Cap
FP
96018-06
62
59
HIC
HdC
StPB
LrC
WB
SWB
Grand Banks of Newfoundland
42
48
SE Grand Banks
SW Grand Banks
Newfoundland Seamounts
Tail of the Bank
87008-07
200 km
B
2001043
2004024
Grand Banks
MD95-2031
37
15
16
35
34
Narwhal Canyon
DesBarres Canyon
10 km
Labrador Current
North Atlantic Current
Transverse Trough
Ice margin 25 ka (max)
Ice margin 25 ka (best)
Ice margin 18.7 ka
TT = Trinity Trough
FP = Flemish Pass
AC = Avalon Channel
WB = Whale Bank
HdC = Haddock Channel
HIC = Halibut Channel
LrC = Laurentian Channel
SWB = South Whale Basin
StPB = St Pierre Bank

Figure 1

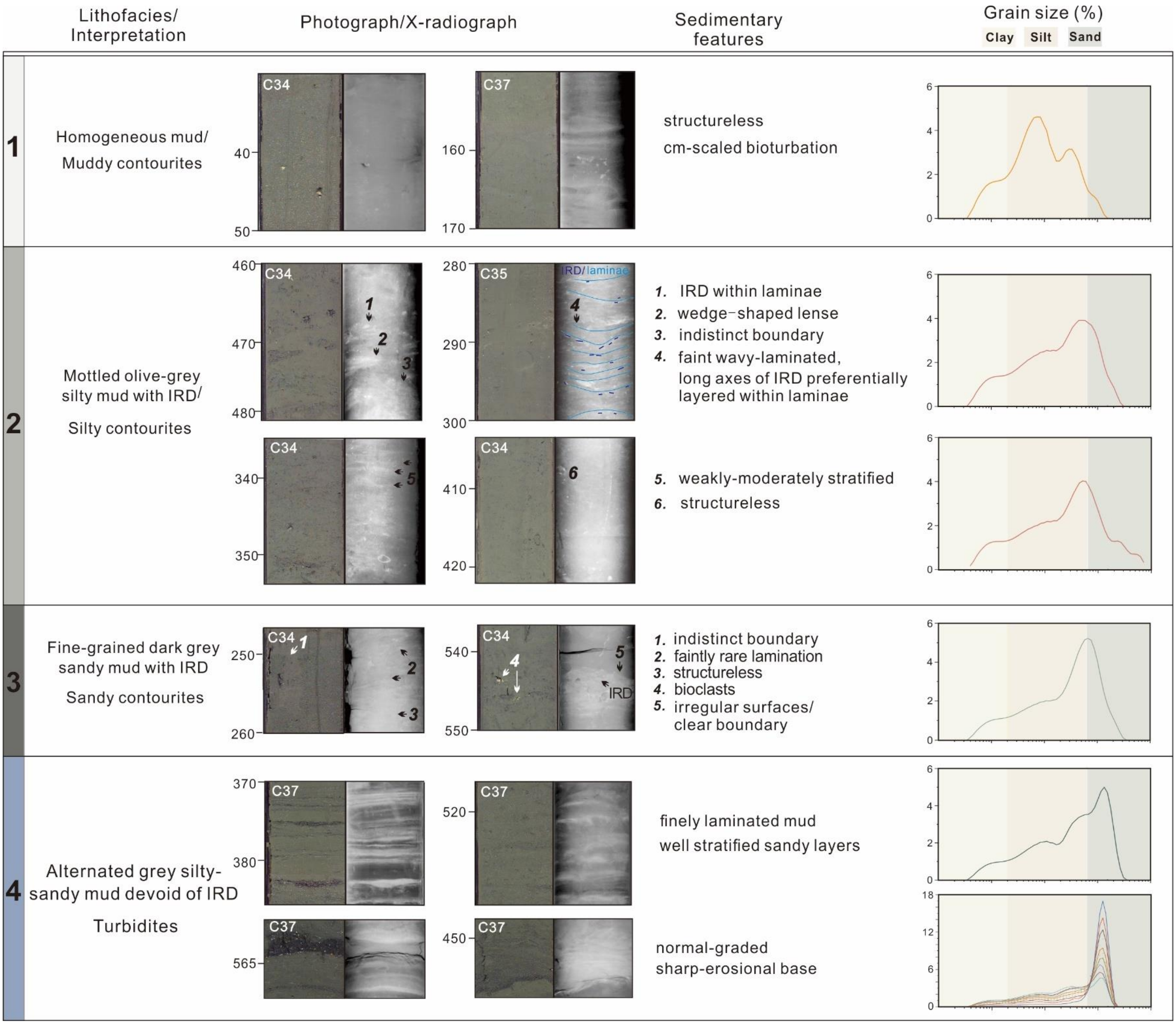

Lithofacies/ Interpretation
Photograph/X-radiograph
Sedimentary features
Grain size (%)
Clay
Silt
Sand
1
Homogeneous mud/ Muddy contourites
C34
C37
structureless
cm-scaled bioturbation
2
Mottled olive-grey silty mud with IRD/ Silty contourites
C35
IRD/laminae
1. IRD within laminae
2. wedge-shaped lense
3. indistinct boundary
4. faint wavy-laminated, long axes of IRD preferentially layered within laminae
5. weakly-moderately stratified
6. structureless
3
Fine-grained dark grey sandy mud with IRD
Sandy contourites
IRD
1. indistinct boundary
2. faintly rare lamination
3. structureless
4. bioclasts
5. irregular surfaces/ clear boundary
4
Alternated grey silty-sandy mud devoid of IRD
Turbidites
finely laminated mud
well stratified sandy layers
normal-graded
sharp-erosional base

Figure 2

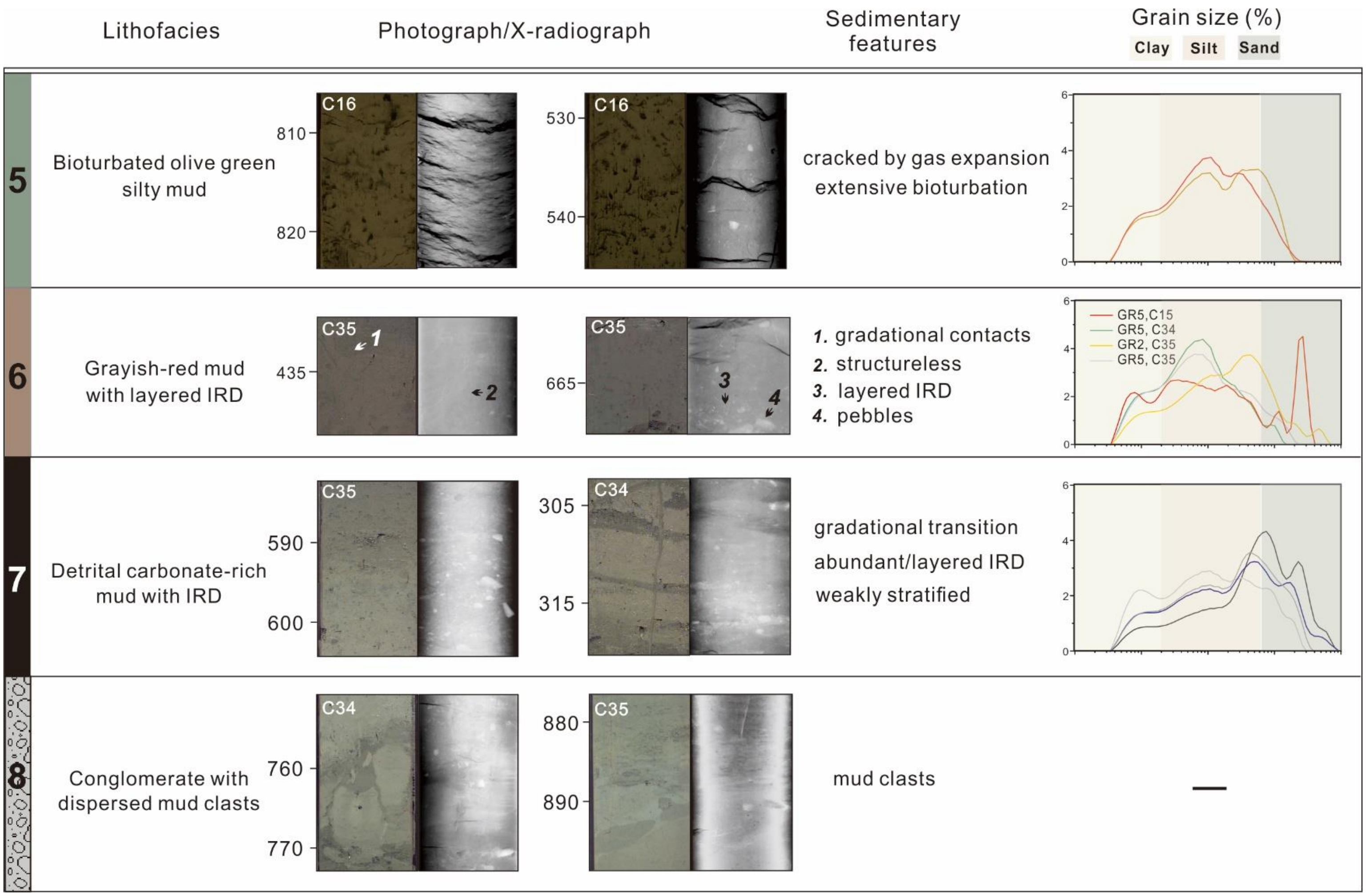

Lithofacies
Photograph/X-radiograph
Sedimentary features
Grain size (%)
Clay
Silt
Sand
5
Bioturbated olive green silty mud
C16
810
820
530
540
cracked by gas expansion
extensive bioturbation
6
Grayish-red mud with layered IRD
C35
435
665
1
2
3
4
1. gradational contacts
2. structureless
3. layered IRD
4. pebbles
GR5,C15
GR5, C34
GR2, C35
GR5, C35
7
Detrital carbonate-rich mud with IRD
C35
590
600
C34
305
315
gradational transition
abundant/layered IRD
weakly stratified
8
Conglomerate with dispersed mud clasts
C34
760
770
C35
880
890
mud clasts
—

Figure 3

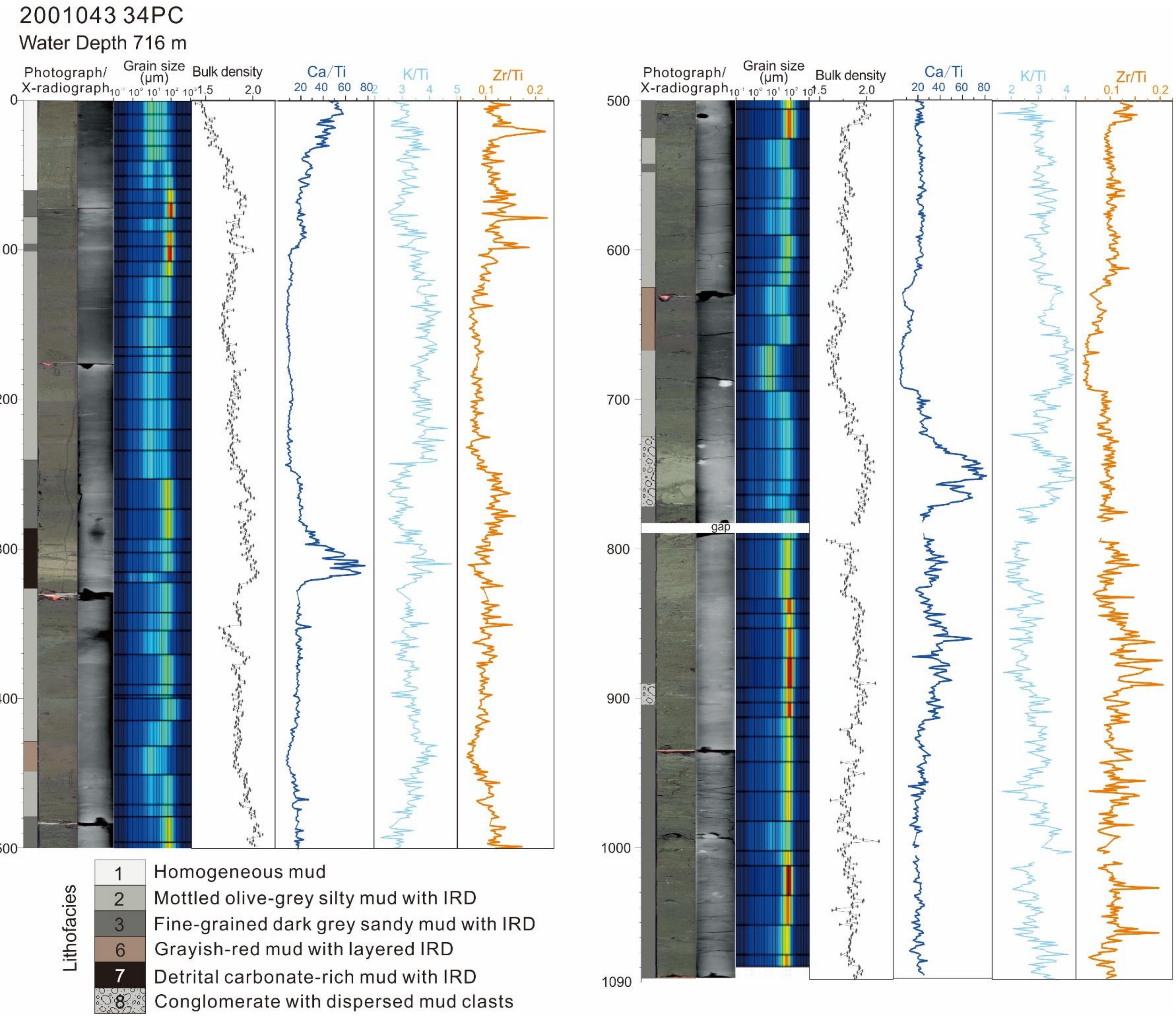

2001043 34PC
Water Depth 716 m
Photograph/ X-radiograph
Grain size (μm)
Bulk density
Ca/Ti
K/Ti
Zr/Ti
gap
Lithofacies
1 Homogeneous mud
2 Mottled olive-grey silty mud with IRD
3 Fine-grained dark grey sandy mud with IRD
6 Grayish-red mud with layered IRD
7 Detrital carbonate-rich mud with IRD
8 Conglomerate with dispersed mud clasts

Figure 4

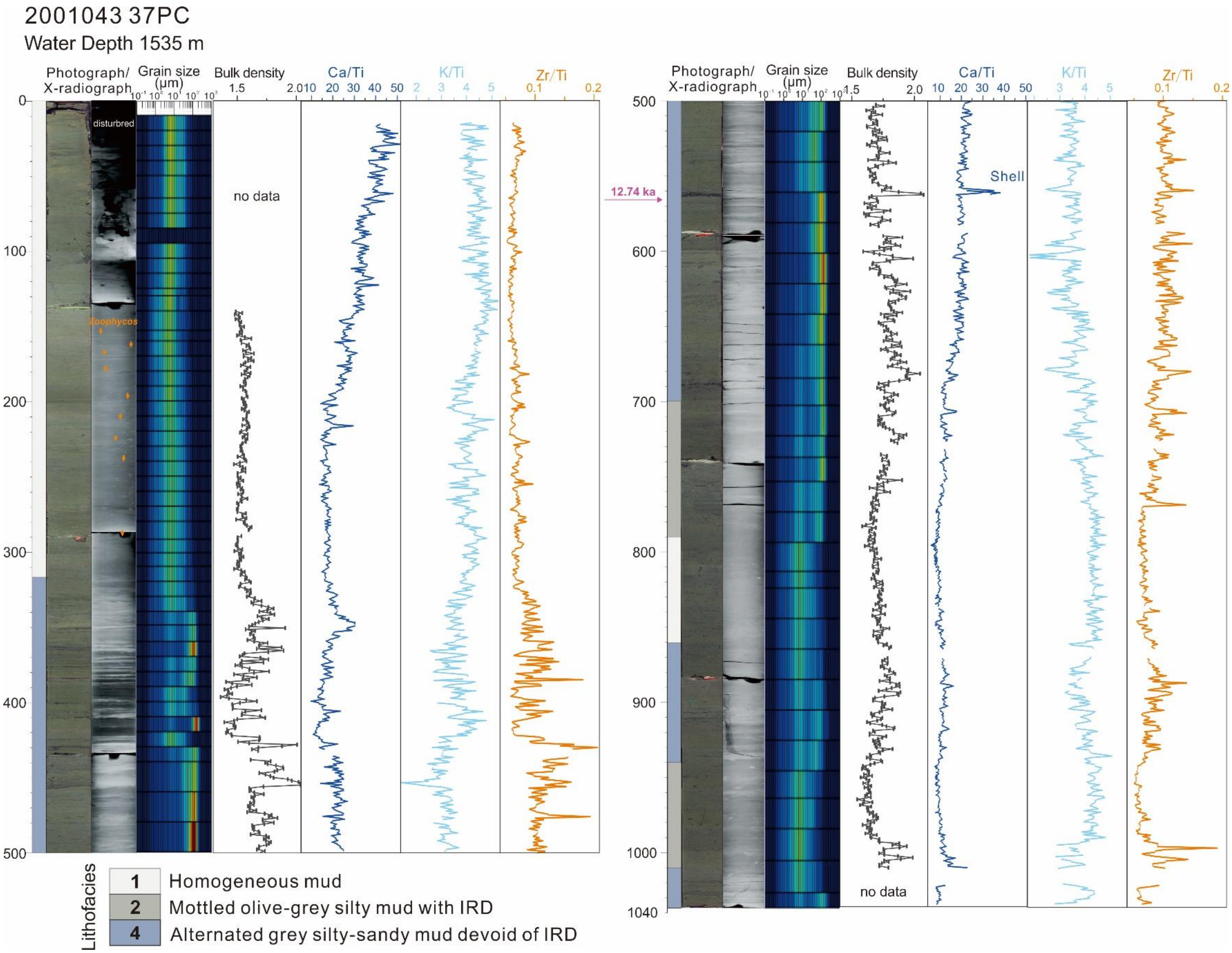
2001043 37PC
Water Depth 1535 m
Photograph/ X-radiograph
Grain size (μm)
Bulk density
Ca/Ti
K/Ti
Zr/Ti
disturbed
Zoophycos
no data
12.74 ka
Shell
Lithofacies
1 Homogeneous mud
2 Mottled olive-grey silty mud with IRD
4 Alternated grey silty-sandy mud devoid of IRD

Figure 5

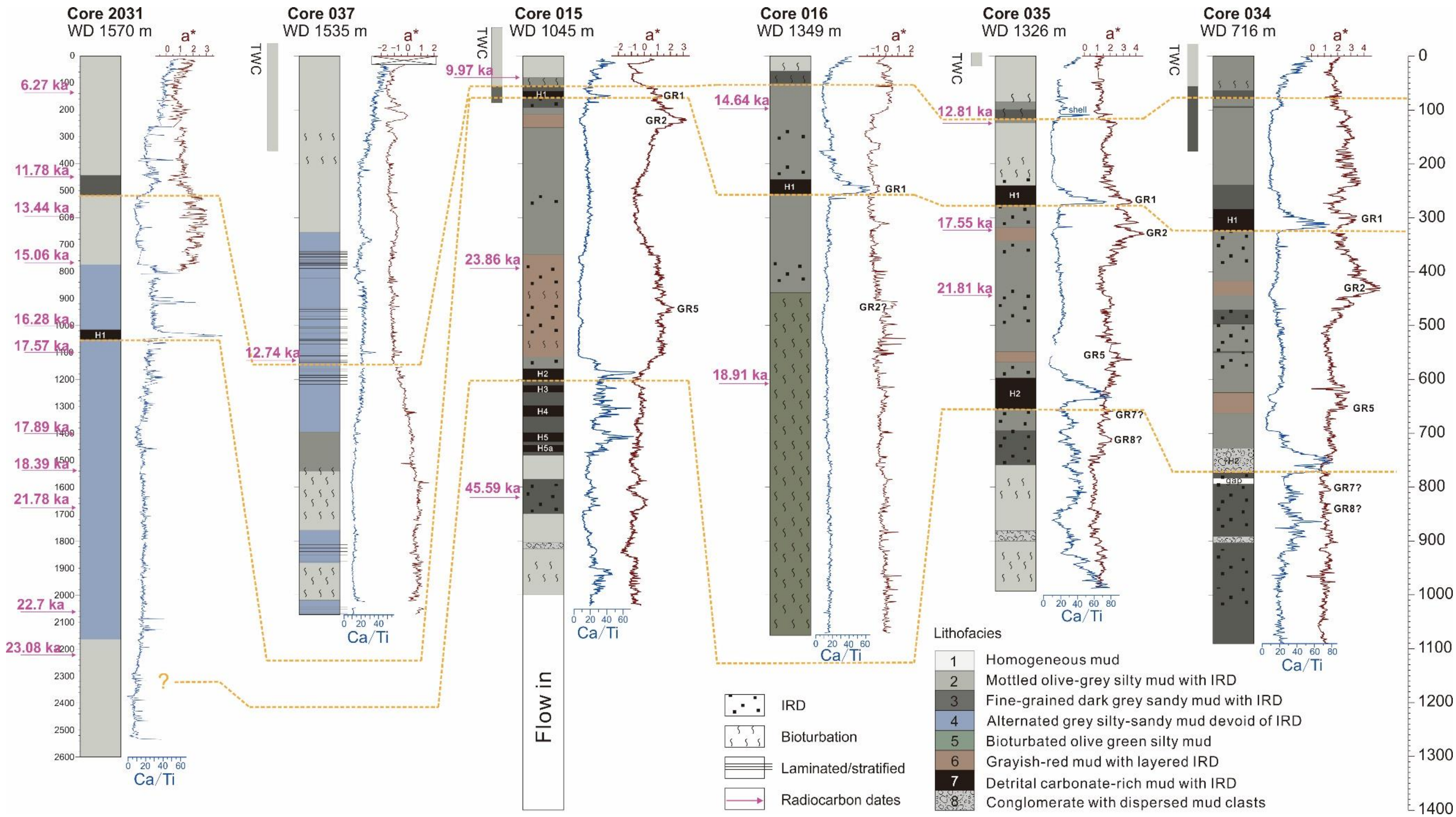
Core 2031
WD 1570 m
Core 037
WD 1535 m
Core 015
WD 1045 m
Core 016
WD 1349 m
Core 035
WD 1326 m
Core 034
WD 716 m
a*
Ca/Ti
TWC
6.27 ka
11.78 ka
13.44 ka
15.06 ka
16.28 ka
17.57 ka
17.89 ka
18.39 ka
21.78 ka
22.7 ka
23.08 ka
12.74 ka
9.97 ka
23.86 ka
45.59 ka
14.64 ka
18.91 ka
12.81 ka
17.55 ka
21.81 ka
H1
H2
H3
H4
H5
H5a
GR1
GR2
GR5
GR2?
GR7?
GR8?
shell
gap
Flow in
IRD
Bioturbation
Laminated/stratified
Radiocarbon dates
Lithofacies
1 Homogeneous mud
2 Mottled olive-grey silty mud with IRD
3 Fine-grained dark grey sandy mud with IRD
4 Alternated grey silty-sandy mud devoid of IRD
5 Bioturbated olive green silty mud
6 Grayish-red mud with layered IRD
7 Detrital carbonate-rich mud with IRD
8 Conglomerate with dispersed mud clasts

Figure 6

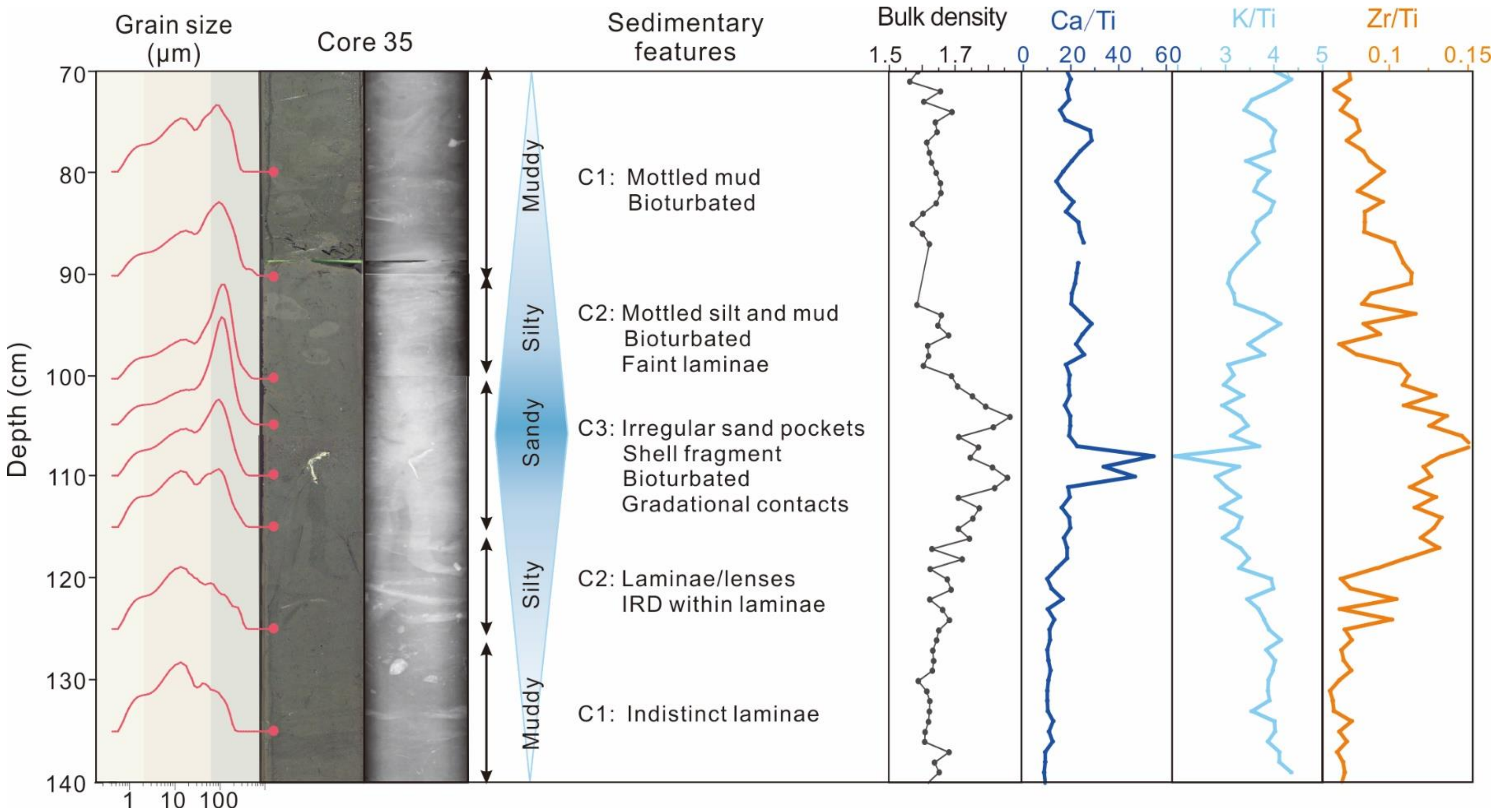
Grain size (μm)
Core 35
Sedimentary features
Bulk density
Ca/Ti
K/Ti
Zr/Ti
1.5 1.7
0 20 40 60
3 4 5
0.1 0.15
Depth (cm)
70
80
90
100
110
120
130
140
1 10 100
Muddy
Silty
Sandy
Silty
Muddy
C1: Mottled mud
Bioturbated
C2: Mottled silt and mud
Bioturbated
Faint laminae
C3: Irregular sand pockets
Shell fragment
Bioturbated
Gradational contacts
C2: Laminae/lenses
IRD within laminae
C1: Indistinct laminae

Figure 7

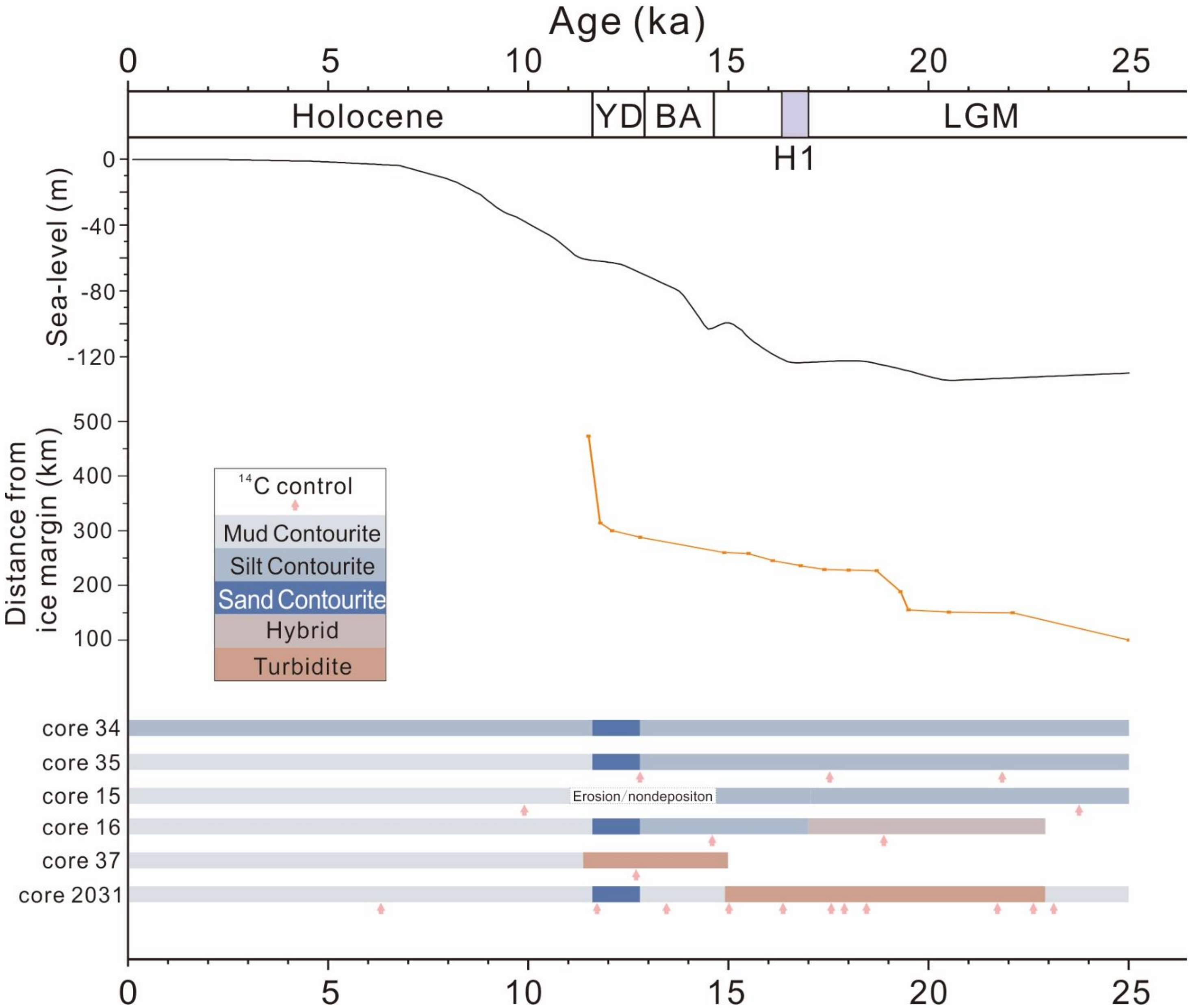

Age (ka)
0
5
10
15
20
25
Holocene
YD
BA
H1
LGM
Sea-level (m)
0
-40
-80
-120
Distance from ice margin (km)
500
400
300
200
100
14C control
Mud Contourite
Silt Contourite
Sand Contourite
Hybrid
Turbidite
core 34
core 35
core 15
Erosion/nondepositon
core 16
core 37
core 2031

Figure 8

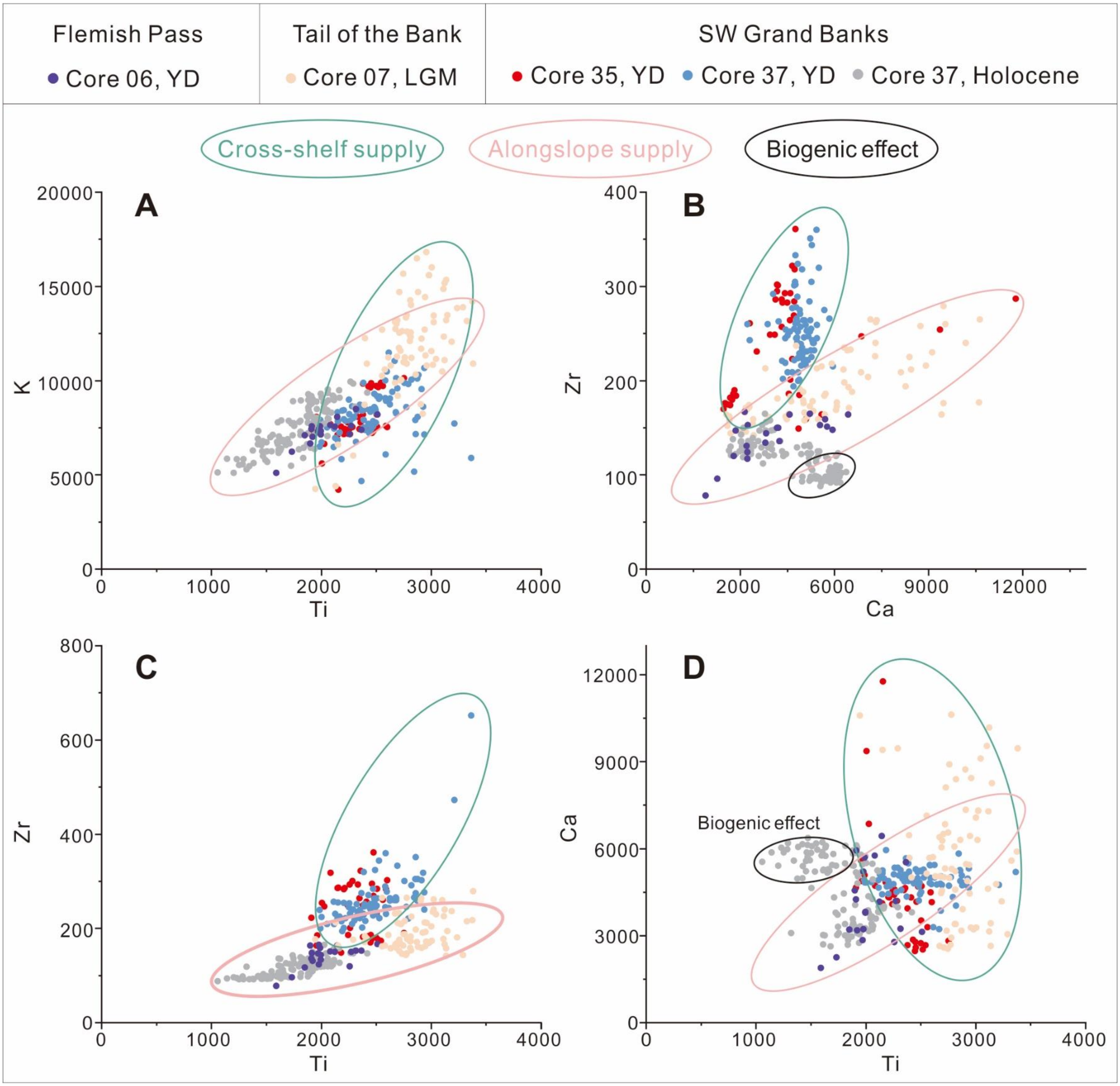
Flemish Pass
Core 06, YD
Tail of the Bank
Core 07, LGM
SW Grand Banks
Core 35, YD
Core 37, YD
Core 37, Holocene
Cross-shelf supply
Alongslope supply
Biogenic effect
A
B
C
D
K
Ti
Zr
Ca
Biogenic effect

Figure 9

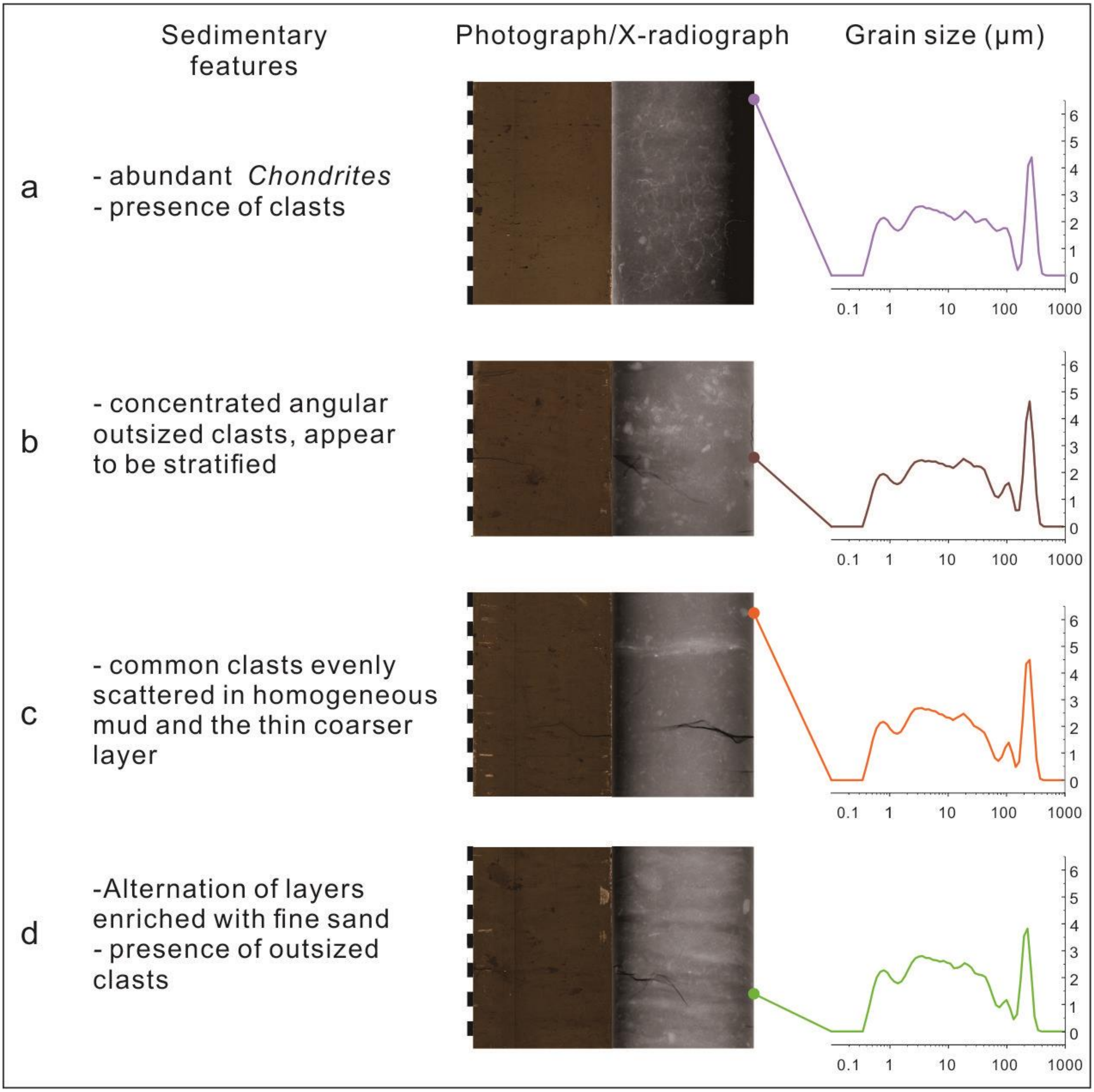
Sedimentary features
Photograph/X-radiograph
Grain size (µm)
a
- abundant *Chondrites*
- presence of clasts
b
- concentrated angular outsized clasts, appear to be stratified
c
- common clasts evenly scattered in homogeneous mud and the thin coarser layer
d
-Alternation of layers enriched with fine sand
- presence of outsized clasts
0.1
1
10
100
1000
0
1
2
3
4
5
6

Figure 10

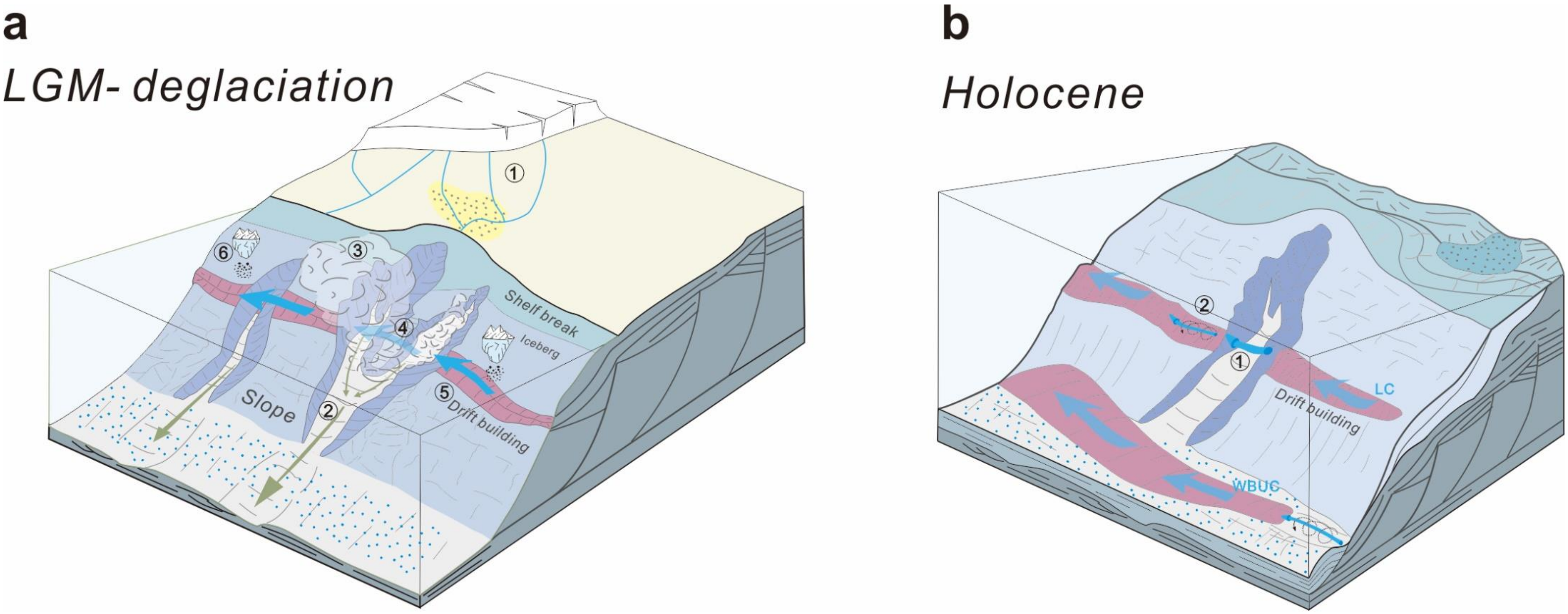
a
LGM- deglaciation
①
⑥
③
Shelf break
④
Iceberg
⑤
Slope
②
Drift building
b
Holocene
②
①
LC
Drift building
WBUC

Figure 11

Table 1

Cores used in this study.

Expedition No.	Core No.	Length (cm)	Water depth (m)	latitude	longtitude
2001043	34	1130	716	44.102	-53.022
	35	1023	1326	44.091	-53.165
	37	1075	1535	44.329	-53.608
2004024	15	1400	1045	44.266	-53.413
	16	1085	1394	44.199	-53.262
MD-95	2031	2772	1570	44.308	-53.736

Table 2

^{14}C-AMS dates used in the study.

Core	Depth (cm)	Uncorrected ^{14}C age year BP	Cal year BP	Materials	Lab ID	Ref
2001043-35	125-126	11610 ± 30	12813.5 ± 155.5	P. Forams	UCI-240236	This study
	320-321	15305 ± 40	17548.5 ± 276.5	P. Forams	UCI-240237	This study
	445	18920 ± 50	21812.5 ± 289.5	Shell	UCI-244642	This study
2004024-15	40-41	9485 ± 20	9973 ± 198	P. Forams	UCI-244635	This study
	395	20770 ± 70	23855.5 ± 267.5	Shell	UCI-244641	This study
	819	43830 ± 970	45589 ± 1714	Shell	TO-12443	Piper et al., 2006
2004024-16	99	13100 ± 30	14644.5 ± 296.5	Bivalve	UCI-240238	This study
	609-611	16545 ± 40	18909.5 ± 219.5	P. Forams	UCI-244636	This study
2001043-37	565	11530 ± 25	12735.5 ± 142.5	Bivalve	UCI-244640	This study
MD 95-2031	148	6190 ± 60	6270.5 ± 209.5	P. Forams	BETA-103557	NRCan database
	448	10640 ± 50	11781.5 ± 256.5	P. Forams	BETA-103558	NRCan database
	598	12260 ± 60	13444.5 ± 213.5	P. Forams	BETA-103559	NRCan database
	770	13360 ± 50	15059 ± 248	P. Forams	BETA-103560	NRCan database
	998	14290 ± 50	16277 ± 266	P. Forams	BETA-103561	NRCan database
	1099	15330 ± 60	17574 ± 295	P. Forams	BETA-103562	NRCan database
	1397	15650 ± 170	17885 ± 479	Shell	TO-6357	NRCan database
	1558	16040 ± 100	18391 ± 286	P. Forams	TO-7001	NRCan database
	1680-1682	18900 ± 70	21778.5 ± 313.5	M.forams	UCI- 250756	This study

	1730	28510 ± 210	31576 ± 475	Shell	TO-5838	NRCan database
	2335	49480 ±1030	52230.5 ± 2759.5	Shell	TO-5837	NRCan database
	2060-2065	19765 ± 50	22703.5 ± 240.5	M.forams	UCI-256024	This study
	2220-2225	20085 ± 50	23078 ± 243	M.forams	UCI-256025	This study

Radiocarbon dates were converted to calibrated years BP using Calib 8.1 and the Marine 20 calibration curve of Heaton et al. (2020) with a ΔR of 144 ± 35.

P. forams = Planktonic foraminifers.

M. forams = Mixed planktonic and benthic foraminifers.

UCI = The University of California at Irvine Keck Carbon Cycle AMS Program.

TO = Isotrace Radiocarbon Laboratory, University of Toronto

BETA = Beta Analytic

NRCan database: https://ed.gdr.nrcan.gc.ca/radiocarbon_e.php